

A Structurally Flexible Halide Solid Electrolyte with High Ionic Conductivity and Air Processability

Guruprakash Karkera,* Mervyn Soans, Ayça Akbaş, Raiker Witter, Holger Euchner, Thomas Diemant, Musa Ali Cambaz, Zhen Meng, Bosubabu Dasari, Shivaraju Guddehalli Chandrappa, Prashanth W. Menezes, and Maximilian Fichtner*

In this work, a structurally revivable, chloride-ion conducting solid electrolyte (SE), $\text{CsSn}_{0.9}\text{In}_{0.067}\text{Cl}_3$, with a high ionic conductivity of $3.45 \times 10^{-4} \text{ S cm}^{-1}$ at 25 °C is investigated. The impedance spectroscopy, density functional theory, solid-state ^{35}Cl NMR, and electron paramagnetic resonance studies collectively reveal that the high Cl^- ionic mobility originates in the flexibility of the structural building blocks, Sn/InCl_6 octahedra. The vacancy-dominated Cl^- ion diffusion encompasses co-ordinated Sn/In(Cl) site displacements that depend on the exact stoichiometry, and are accompanied by changes in the local magnetic moments. Owing to these promising properties, the suitability of the $\text{CsSn}_{0.9}\text{In}_{0.067}\text{Cl}_3$, as an electrolyte is demonstrated by designing all-solid-state batteries, with different anodes and cathodes. The comparative investigation of interphases with Li, Li–In, Mg, and Ca anodes reveals different levels of reactivity and interphase formation. The $\text{CsSn}_{0.9}\text{In}_{0.067}\text{Cl}_3$ demonstrates an excellent humidity tolerance (up to 50% relative humidity) in ambient air, maintaining high structural integrity without compromises in ionic conductivity, which stands in contrast to commercial halide-based lithium conductors. The discovery of a halide perovskite conductor, with air processability and structure revival ability paves the way for the development of advanced air processable SEs, for next-generation batteries.

1. Introduction

Redox reactions of transition metals are the key players for the charge transfer in lithium-ion batteries (LIBs).^[1] As new developments are unveiling, anionic redox has been found to be contributing to the overall capacity generated in LIBs.^[2] In advanced Li–O₂ batteries, lithium halides are known to be efficient redox mediators that minimize the charging overpotential.^[3] On the other hand, solid electrolytes (SEs) are a rapidly developing area in LIB, where increased attention has been received by halide containing SEs, which display enhanced stability at metal interphases.^[4] Zhou et al. reported a chloride-based fast Li-ion conductor $\text{Li}_2\text{In}_x\text{Sc}_{0.666-x}\text{Cl}_4$, which has shown high areal capacity and cyclability, with $\text{LiCoO}_2/\text{LiNi}_{0.85}\text{Co}_{0.1}\text{Mn}_{0.05}\text{O}_2$ cathodes.^[5] The incorporation of halide ions enhances the functionality of SEs in lithium metal batteries. Due to their

G. Karkera, M. Soans, A. Akbaş, R. Witter, T. Diemant, M. A. Cambaz, Z. Meng, S. G. Chandrappa, M. Fichtner
Helmholtz Institute Ulm (HIU) Electrochemical Energy Storage
Helmholtzstrasse 11, 89081 Ulm, Germany
E-mail: karkera.guruprakash@uni-ulm.de; m.fichtner@kit.edu
R. Witter, B. Dasari, M. Fichtner
Institute of Nanotechnology (INT)
Karlsruhe Institute of Technology (KIT)
Hermann-von-Helmholtz Platz 1, 76344 Eggenstein-Leopoldshafen, Germany

R. Witter
Institute of Quantum Optics
Ulm University
Albert-Einstein-Allee 11, 89081 Ulm, Germany
R. Witter
Department of Cypernetics
Tallinn University of Technology (TalTech)
Ehitajate tee 5, Tallinn 19086 Estonia
H. Euchner
Institute of Physical and Theoretical Chemistry
Auf der Morgenstelle 15, 72076 Tübingen, Germany
P. W. Menezes
Materials Chemistry Group for Thin Film Catalysis–CatLab
Helmholtz-Zentrum Berlin für Materialien und Energie
Albert-Einstein-Str. 15, 12489 Berlin, Germany
P. W. Menezes
Department of Chemistry
Technical University of Berlin
Straße des 17 Juni 135. Sekr. C2, 10623 Berlin, Germany

 The ORCID identification number(s) for the author(s) of this article can be found under <https://doi.org/10.1002/aenm.202300982>

© 2023 The Authors. Advanced Energy Materials published by Wiley-VCH GmbH. This is an open access article under the terms of the Creative Commons Attribution-NonCommercial-NoDerivs License, which permits use and distribution in any medium, provided the original work is properly cited, the use is non-commercial and no modifications or adaptations are made.

DOI: 10.1002/aenm.202300982

inherently high stability against oxidation (≈ 4.0 V vs Li^+/Li), compared to sulfide-based SEs (≈ 2.5 V),^[6] chloride SEs have attracted increasing interest.^[7] With Cl being more electronegative than S, generally oxidation potentials of chloride-based SE are much higher than those of sulfide SEs.^[4] The chemical compatibility of SEs with both cathode active material (CAM) and metallic anodes is another critical aspect, in order to obtain long life, safer, and high-energy all-solid-state batteries (ASSBs). In this perspective, chloride-based SEs were found to have better chemical stability with many CAMs.^[8] Recently, Na/Cl₂ and Li/Cl₂ batteries have been developed, which use an AlCl₃:SOCl₂-based electrolyte and a carbon-based cathode.^[9] The exponential growth in the cost of LIB raw materials has increased the scope for realizing batteries beyond lithium systems, such as Na-ion^[10] or multivalent/anion shuttle-based batteries.^[11] Anionic batteries solely depend on the charge transfer via anionic shuttle, originating from halide-based electrode materials. In particular, chloride-ion batteries (CIBs) attracted increasing interest, in the recent years, due to their high theoretical energy densities and the abundance of chloride-based materials. Despite wide range of available chloride-based materials, their application in batteries is limited due to inherent solubility of metal chlorides in most solvents. Novel engineering of the electrode and electrolyte is the need of the hour to overcome the solubility challenge. Hence, developing chloride-based SEs would benefit CIBs in two ways; first, it would overcome the electrode solubility issues and second, it would open pathways to employ a wide range of cathode materials. In the past, Gschwind et al. developed chloride-ion conducting polymer membranes of gelatin, polyvinyl chloride, and polyvinylidene fluoride-hexafluoropolymer.^[12] Following this, Chen et al. developed a polyethylene oxide-based polymer electrolyte, with demonstrated chloride-ion cycling at room temperature (RT).^[13] Later, Nunotani et al. showed that Ca²⁺ doping enhances the conductivity of LaOCl-based SEs.^[14] Sakamoto et al. reported Pb_{1-x}K_xCl_{2-x} as a chloride-ion conductor and showed electrochemical battery cycling at 160 °C.^[15] Murin et al. has examined CsSnCl₃ (CSC), SnCl₂, and PbCl₂ as promising solid chloride-ion conductors.^[16] The cubic perovskite CsSnCl₃ has shown good Cl⁻ ionic conductivity, yet, it only exists as a metastable phase at RT. Later on, Xia et al. were able to stabilize the cubic CsSnCl₃ structure by thermal treatment after mechanical milling.^[17] However, this report lacks comprehensive structural/electrochemical studies. More importantly, the long-term stability of thermally treated CSC is unclear. A stable structured, ambient air processable inorganic electrolyte, capable of shuttling chloride ions at RT has not been reported so far. Herein, we show that the cubic perovskite CsSnCl₃ can be stabilized by a B site substitution with In³⁺. The In³⁺-doped CsSn_{0.9}In_{0.067}Cl₃ (CSIC) was synthesized by mechanical milling and characterized by various physical and chemical methods, demonstrating its structural integrity and the preservation of the perovskite structure.

Impedance spectroscopy (EIS) and linear sweep voltammetry (LSV) reveal that as-prepared CSIC exhibits a chloride-ion conductivity of 3.2×10^{-4} S cm⁻¹ at RT and a wide electrochemical stability window of ≈ 5.3 V versus stainless steel (SS). The electrolyte was combined with WOCl₄ as CAM and a Li metal anode (LMA) in a full-cell, with the resulting ASSB delivering a reversible capacity of 82 mAh g⁻¹ after 20 cycles. The excellent RT ionic mobility of the SE allows the use of the untapped class of

common metal chlorides (such as VCl₃, which is soluble in liquid electrolytes) as CAM, which up to now had been ruled out for the use in CIB.

2. Results and Discussion

2.1. Synthesis and Characterization of SE

Figure 1a shows the X-ray diffraction (XRD) patterns of the as-prepared CSC, CSIC, and heat-treated CSC (CSC-HT) samples recorded after different storage times. The vividly yellow colored, perovskite cubic CSC (c-CSC) is a metastable phase and tends to transform to a stable, monoclinic phase (m-CSC, white in color), during the resting periods of a few days even at inert conditions.^[18] The reason for this metastability is the imbalanced ionic radii of the Cs⁺, Sn²⁺, and Cl⁻, with a resultant tolerance factor $t = 0.87$, which is smaller than the lower limit for the formation of the cubic perovskite structure of 0.9 (details are given in the Supporting Information). A substitution by either a larger cation than Cs⁺ or a smaller cation than Sn²⁺ could, however increase it to 0.90 and thus stabilize the cubic phase.^[19] Hence, the substitution of 0.067 moles of In³⁺ into the Sn²⁺ site not only creates a stabilized cubic structure but due to charge balancing arguments also results in the formation of Sn vacancies in the structure of CsSn_{0.9}In_{0.067}Cl₃.^[18] CSIC possesses a similar yellow color and remains physically and structurally unaltered under argon atmosphere even after 6 months, as confirmed by XRD. The details on its air and humidity tolerance are discussed in Section 2.6.

Raman spectroscopy is a unique technique to differentiate the nature of bonds involved in the structure, particularly differences due to the B site (Sn/In) occupancy can be resolved, as shown in Figure 1b. The monoclinic structure (m-CSC) is considered to be formed by Cs⁺ and SnCl₃⁻ ions,^[20] thus showing symmetric and asymmetric stretching of Sn–Cl₃⁻ from terminal Sn–Cl₃⁻ bonds. The ν_1 (A_g) mode is the totally symmetric stretching of SnCl₃⁻ ions in the unit cell and gives rise to the strongest Raman band at 165 cm⁻¹, while, its shoulder at 145 cm⁻¹ corresponds to the other ν_1 mode of B_g symmetry. There are three asymmetric, stretching vibrations observed for the ν_3 modes, located at ≈ 227.9 , 249.4, 264.2 cm⁻¹, respectively, and an additional weak vibration at 278.6 cm⁻¹. The phase conversion from cubic to monoclinic or vice-versa is manifested by a color change (yellow to white), as well as the disappearance of the Raman active modes for the centrosymmetric c-CSC, meaning that no vibrational modes are observed. When the center of symmetry is destroyed, the structure turns back to monoclinic phase and the Raman active bands reappear. CSIC displayed no Raman active bands except the symmetric In³⁺–Cl stretching feature at 281 cm⁻¹.^[18] Additionally, both cubic phases were accompanied by a fluorescent background between 100 and 150 cm⁻¹. As observed in the XRD results in Figure 1a, after different storage times, the c-CSC and CSC-HTs structures have changed/accompanied monoclinic phase, while CSIC retained its cubic structure for longer storage times. The c-CSC has an ionic conductivity in the order of 10⁻⁴ S cm⁻¹ at RT, which drops to 10⁻⁶ S cm⁻¹ upon phase change to the monoclinic phase,^[16,18] i.e., the phase change comes with the loss of its good ionic conductivity. The m-CSC phase can be transformed back to c-CSC by a 2 h heat treatment

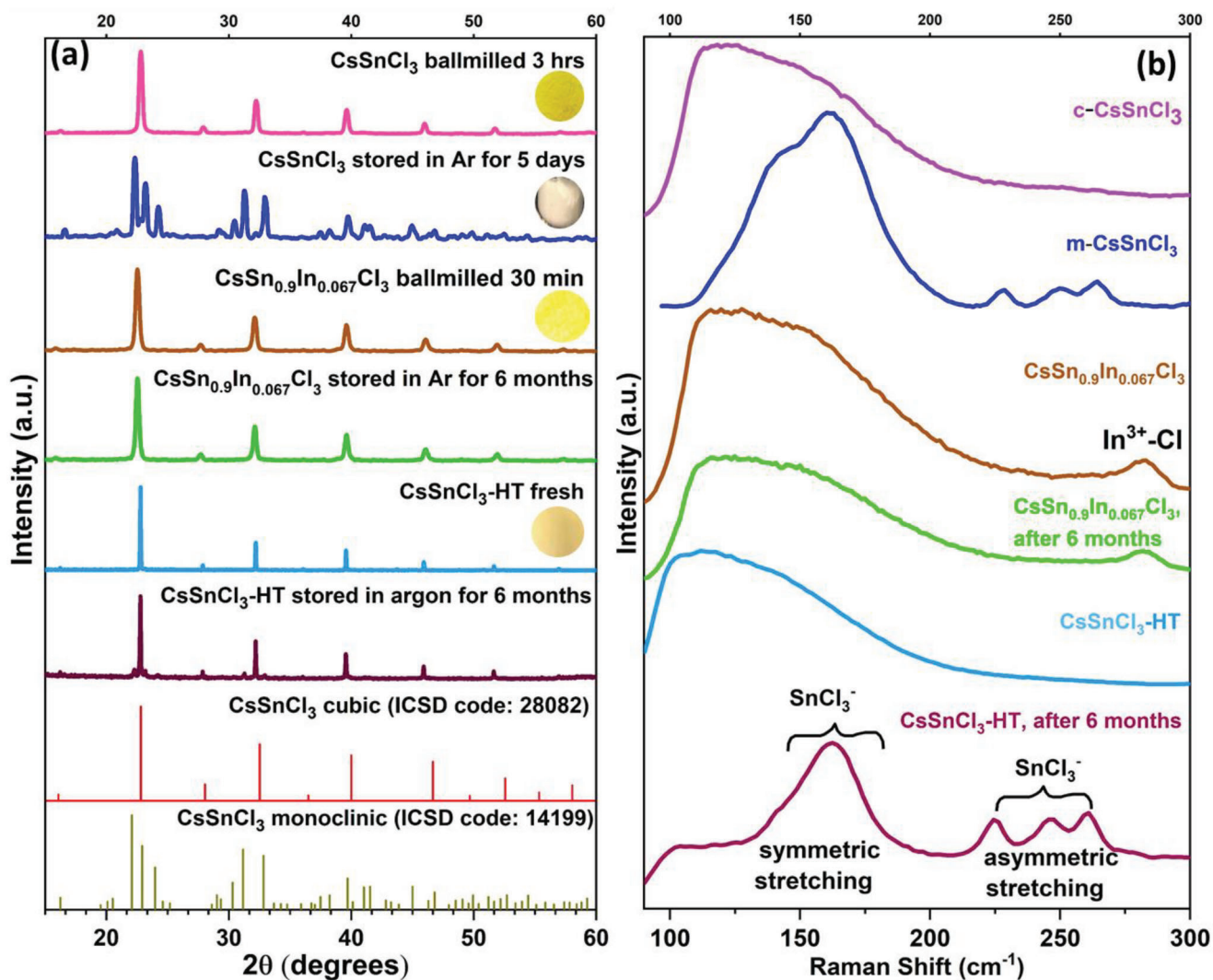


Figure 1. a) X-ray diffractograms of CsSnCl₃ and CsSn_{0.9}In_{0.067}Cl₃:CsSnCl₃ ball milled for 3 h (pink), stored in Ar for 5 days (blue), CsSn_{0.9}In_{0.067}Cl₃ ball milled for 30 min (brown), stored in Ar for 6 months (green), CsSnCl₃-HT (140 °C/2 h in vacuum, light blue) and stored in Ar for 6 months (purple). For comparison: ICSD patterns of cubic CsSnCl₃ (red) and monoclinic CsSnCl₃ (gray), insets show the corresponding sample colors; b) comparison of Raman spectra of cubic CsSnCl₃ (pink), monoclinic CsSnCl₃ (blue), and CsSn_{0.9}In_{0.067}Cl₃ (brown), CsSn_{0.9}In_{0.067}Cl₃ after 6 months storage in Ar atmosphere (green), CsSnCl₃-HT and corresponding pattern after 6 months of storage time in Ar (violet).

at 140 °C in vacuum (dark yellow), however, when stored for long duration (6 months), it partially converts back to the monoclinic structure (Figure S3, Supporting Information), yielding mixed phases, as confirmed by XRD (Figure 1).

Structural analysis of CSIC and c-CSC was performed by Rietveld refinement of the corresponding XRD patterns as shown in Figure 2a and Figure S1 in the Supporting Information. The average crystallite size of CSIC calculated from the XRD reflections (110), (200), and (211) was estimated to be ≈21 nm. The observed Bragg peaks indicate that the material crystallizes in space group *Pm-3m* with a lattice parameter of $a = b = c = 5.56$ Å ($\alpha = \beta = \gamma = 90^\circ$), yielding a unit cell volume of 172.481 Å³, which is slightly smaller than c-CSC, with a $V/Z = 174.1$ Å³ (Table S1, Supporting Information). This means a cubic structure similar to the parent compound CsSnCl₃ (*Pm-3m* space group) is observed.^[18,20] The Wyckoff positions and site occupancy factors

of the individual ions constituting CSIC are given in Table S1 in the Supporting Information. The reduction in the unit cell volume is likely due to the smaller In³⁺ ions in B site. Successful incorporation of indium in Sn²⁺ site is further verified by inductively coupled plasma optical emission spectroscopy (ICP-OES), energy-dispersive X-ray spectroscopy (EDX, Figure S4 and Table S2, Supporting Information), and by In³⁺-Cl stretching feature at 281 cm⁻¹ observed via Raman spectroscopy (Figure 1b). Figure 2b shows the crystal structure of CSIC, where Cs atoms (black), Sn/In (red/yellow), and chloride (orange) are arranged such that each Cs atom is bonded to the eight (Sn/In) Cl₆ octahedra, located at the corners of the cubic structure. For comparison, Figure S3 in the Supporting Information shows the monoclinic crystal structure of CSC, where SnCl₃⁻ trigonal pyramidal arrangements are bonded to Cs⁺ ions, in space group of *P2₁/c*.

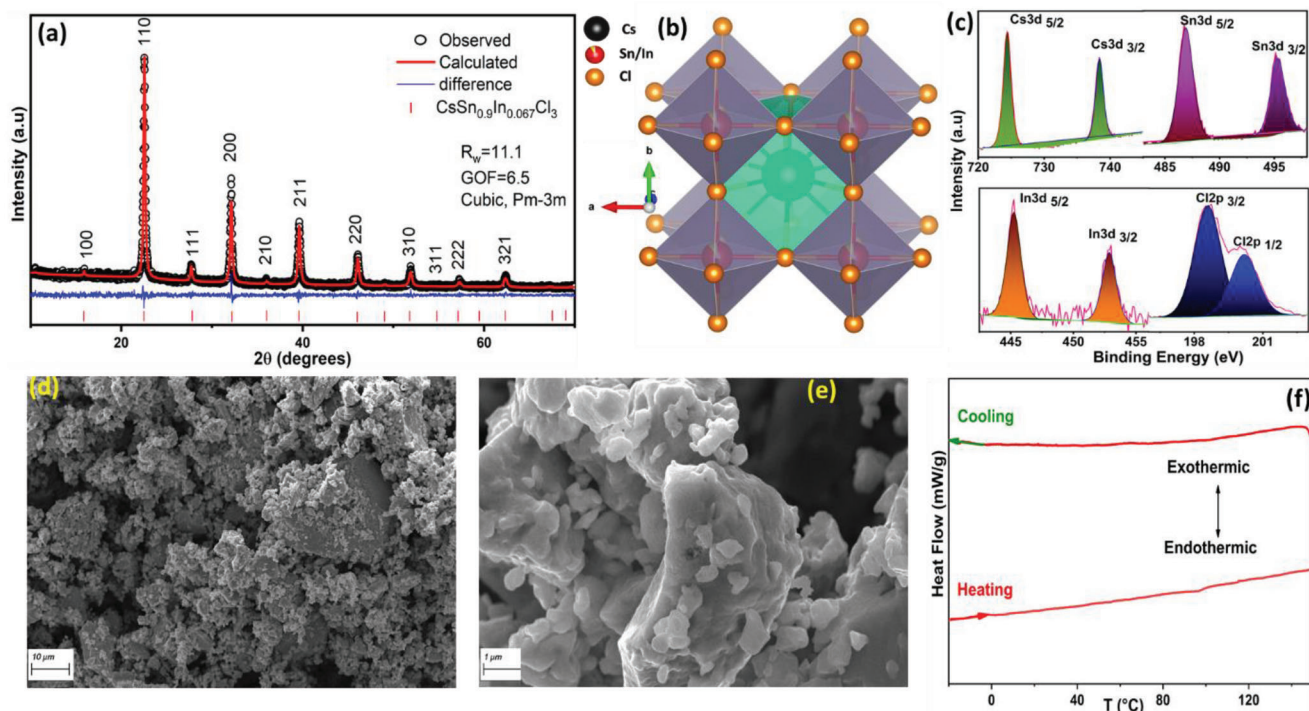


Figure 2. a) Rietveld refined pattern of the X-ray diffraction data of the $\text{CsSn}_{0.9}\text{In}_{0.067}\text{Cl}_3$, b) crystal structure of $\text{CsSn}_{0.9}\text{In}_{0.067}\text{Cl}_3$, with Cs (black), Sn/In (red/yellow), and Cl (orange) atoms, c) XPS detail spectra in the Cs 3d, In 3d, Sn 3d, Cl 2p regions, d,e) FESEM images of as-synthesized CSIC at 10 and 1 μm magnifications, f) DSC of $\text{CsSn}_{0.9}\text{In}_{0.067}\text{Cl}_3$ within the temperature range of -10 and 150 $^{\circ}\text{C}$.

The chemical state of the elements at the surface of the as-prepared solid electrolyte was investigated by X-ray photoelectron spectroscopy (XPS) measurements (Figure 2c). The spectrum in the Cs 3d region showed single peak doublet at binding energies (BEs) of 724.4 eV (Cs $3d_{5/2}$) and 738.4 eV (Cs $3d_{3/2}$), which can be assigned to Cs^+ ,^[21] while the Sn 3d peak doublet was observed at 486.9 eV ($3d_{5/2}$) and 495.3 eV ($3d_{3/2}$) corresponding to Sn^{2+} .^[17,22] Furthermore, the existence of In^{3+} was confirmed by the In 3d peak doublet at 445.3 eV (In $3d_{5/2}$) and 452.9 eV (In $3d_{3/2}$).^[23] Finally, the presence of Cl^- in the material leads to the peak doublet at 198.6/200.2 eV in the Cl 2p region.^[17] Hence, the oxidation states of all elements met the expectations based on the design principle of $\text{CsSn}_{0.9}\text{In}_{0.067}\text{Cl}_3$.

Scanning electron microscopy (SEM) of CSIC indicates particles with an average particle size of 570 nm and large secondary particles formed by agglomeration, having an average size of 4.5 μm (Figure 2d,e). The difference in the crystallite size obtained from the XRD pattern and the SEM image may be due to the predominance of particles in an agglomerated state. EDX spectra (Figure S4a, Supporting Information) of CSIC revealed the stoichiometry of Cs:Sn:In:Cl as 20.13:18.12:1.35:60.40 (an atomic %). For comparison, the SEM image of pristine CsSnCl_3 and the corresponding EDS spectrum are also shown in Figure S4b,c in the Supporting Information, respectively. To know the crystallization effects of heat treatment, the SEM images of CSIC-HT samples are shown in Figure S4d,e in the Supporting Information. The heated sample indicated a similar morphology to CSIC, but with a slightly enhanced aggregation and integration of particles. A differential scanning calorimetry (DSC)

measurement was performed to identify the stable temperature range in which conductivity measurements could be performed on cubic CSIC. As shown in Figure 2f, DSC revealed no phase transitions in the temperature range of -10 to 150 $^{\circ}\text{C}$.

2.2. Chloride-Ion Conductivity Measurements

Ionic conductivities (σ) of the cubic CsSnCl_3 -HT, $\text{CsSn}_{0.9}\text{In}_{0.067}\text{Cl}_3$, and $\text{CsSn}_{0.9}\text{In}_{0.067}\text{Cl}_3$ -HT samples were determined from the Nyquist plots, at RT (Figure 3a) and were found to be 2.5×10^{-4} , 3.2×10^{-4} , and 3.45×10^{-4} S cm^{-1} , respectively. The Nyquist plots were fitted using a resistor and two constant phase elements (CPE, inset in Figure 3a). Here, the bulk and grain boundary resistance could not be differentiated, therefore, resistance R_1 was attributed to the combined bulk and grain boundary resistance with the corresponding constant phase element, CPE_1 . The parallel combination of R_1 and CPE_1 results in a semi-circle in the high-frequency region, while the blocking behavior of the carbon in the low-frequency region (tail) was represented by the second constant phase element CPE_2 . The activation energy (E_a) for the ionic transport was derived from the temperature-dependent Nyquist plots of CSIC measured in the temperature range 25 to 60 $^{\circ}\text{C}$ and is found to be 0.22 eV (Figure 3b). This result is in good agreement with the activation barriers of chloride-ion hopping, obtained from theoretical calculations, which are provided in Section 2.4.

From the application stance of CSIC as an SE, the other important parameter to be measured is its electronic conductivity.

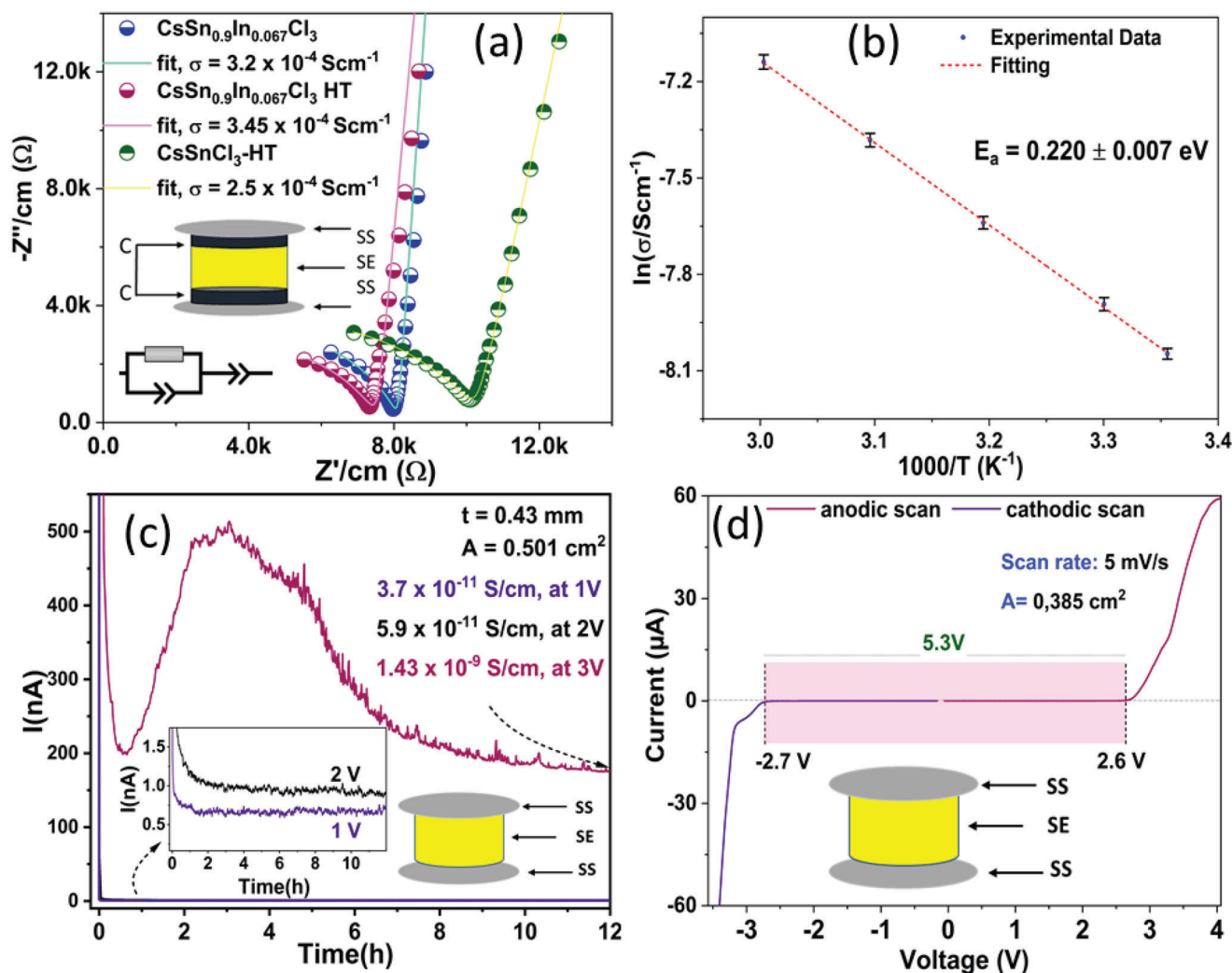


Figure 3. a) Nyquist plots of the cubic $\text{CsSnCl}_3\text{-HT}$, $\text{CsSn}_{0.9}\text{In}_{0.067}\text{Cl}_3$, and $\text{CsSn}_{0.9}\text{In}_{0.067}\text{Cl}_3\text{-HT}$ (symbols) and the corresponding fits (lines), inset: equivalent circuit used for the fit, b) Arrhenius plot of the $\text{CsSn}_{0.9}\text{In}_{0.067}\text{Cl}_3$ sample, c) chronoamperometry plot of $\text{CsSn}_{0.9}\text{In}_{0.067}\text{Cl}_3$ at 1, 2, and 3 V for 12 h each, to estimate the electronic conductivity, d) Linear sweep voltammogram of the $\text{CsSn}_{0.9}\text{In}_{0.067}\text{Cl}_3$ electrolyte within the potential range -3.5 to 4.0 V versus SS. The cell configurations are schematically depicted in all cases, as insets and measurements were carried at RT, except for (b).

This was determined by a DC polarization test, by applying DC voltages of 1, 2, and 3 V for 12 h each (Figure 3c) to CSIC pellets sandwiched between SS blocking electrodes. CSIC displays a low electronic conductivity of $3.7 \times 10^{-11} \text{ S cm}^{-1}$ at 1 V, $5.9 \times 10^{-11} \text{ S cm}^{-1}$ at 2 V, which corroborates its insulating behavior. At 3 V, the curve indicated uneven higher currents (up to ≈ 500 nA, in comparison to ≈ 1 nA at 2 V), likely due to decomposition reactions, with a slight increase in the electronic conductivity to $1.43 \times 10^{-9} \text{ S cm}^{-1}$. This hints that the electrochemical stability regime of CSIC is limited between 2 and 3 V versus SS. The voltage window of CSIC was further assessed using an anodic and cathodic LSV scans versus SS, Li/Li⁺, Mo, and Sn reference electrodes (Figure 3d and Figure S7, Supporting Information), yielding values of ≈ 5.3 , 4.1, 5.3, and 3.0 V, respectively. The LSV versus SS revealed a decomposition after 2.6 V, which corroborates well, with slight increase in the electronic conductivity measurement at 3 V (Figure 3c). Its wider voltage window and lower electronic/higher ionic conductivity enable the exploration of this

electrolyte with a large number of untapped classes of electrode materials for CIBs. The chemical and electrochemical stability behavior of CSIC with different reference electrodes is discussed in detail in Section 2.7.

2.3. Solid-State Magic Angle Spinning (MAS) ³⁵Cl NMR and Electron Paramagnetic Resonance (EPR)

To probe the origin of the observed ionic conductivity enhancement, high-resolution solid-state ³⁵Cl NMR was applied. Commonly, the quadrupolar coupling ($I = 3/2$) for perovskite-like structures varies according to the chloride-ion coordination number (CN). In the case of a low CN structure, like Cs_2SnCl_6 (CN = 1), the quadrupolar coupling (C_Q) has been derived to be as large as 32 MHz.^[22] Further, for CsPbCl_3 with a planar-quadratic symmetry (CN = 4), $|C_Q|$ may range from 29 to 16 MHz, while for CN = 2 (e.g., CsPb_2Cl_5), $|C_Q|$ has been confirmed to be

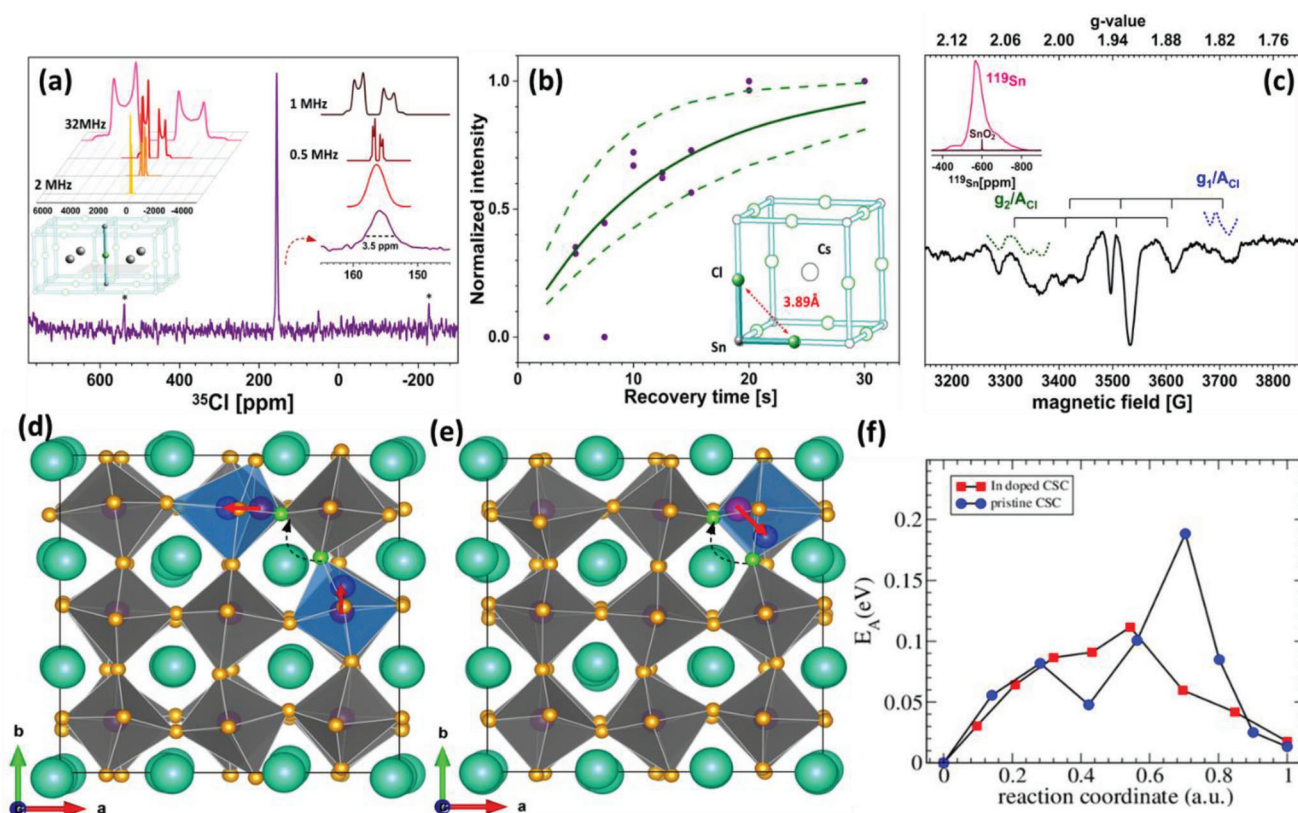


Figure 4. a) Solid-state ^{35}Cl NMR 1D MAS experimental spectrum (purple) and line-shape limit simulations (colored insets): The $\text{CsSn}_{0.9}\text{In}_{0.067}\text{Cl}_3$ resonance appears at 156 ppm (110 ppm in respect to IUPAC referencing). The 2+4 coordination of the chloride ions is made visible with the crystal model. SIMPSON line-shape limit simulations show that only an effective <0.5 MHz, can lead to a line width of 3.5 ppm. Spinning sidebands are indicated by a star (*), b) the longitudinal relaxation curve obtained by saturation recovery provides a relative long T_1 time of 12(6) s. In c), the EPR spectrum of CSIC presents the interaction of unpaired electron contributions with nearby short-lived $^{35,37}\text{Cl}$ nuclei. As abscissa, the dimensionless effective electron magnetic moment g is used. Contributions from In and Sn were not detected with the X-band equipment due to exceeding hyperfine coupling strengths. However, the paramagnetically broadened ^{119}Sn NMR 1D MAS spectrum of CSIC is shown with SnO_2 as a diamagnetic reference. DFT studies of $3 \times 3 \times 3$ supercells of d) pristine CSC and e) In-doped CSC used for the assessment of the diffusion barriers for a Cl-ion diffusing to a vacant site. The light orange atoms represent chloride, while In/Sn are located inside the Cl-octahedra. The light green atoms depict the initial and final position for a Cl diffusion process, with the dashed arrow indicating the diffusion path. The pink/blue atoms in the blue octahedra show d) two Sn, e) one In atom and their respective displacements during the diffusion process (indicated by the red arrow) atoms connecting initial and final state of a diffusion event. In (f), the minimum energy path for the diffusion processes in (d) and (e) are depicted.

around 14 MHz.^[23] In the case of CSIC, we have an asymmetric coordination of 2+4 = 6, consisting of a Cl-Sn₂-linear (Cl-Sn distance of $\approx 2.8 \text{ \AA}$) and a Cl-Cs₄-square-planar coordination (Cl-Cs distance of $\approx 3.9 \text{ \AA}$). Both are contributing to the electric field gradient (the EFG being the second derivative of the electric potential of the electron distribution $\partial^2 V / \partial x_i^2$ with respect to the principal axis system coordinates, $x_i = x, y, z$). Accordingly, a value from 14 to 32 MHz could be expected. Here, we determined the EFG of CSIC from density functional theory (DFT, see Section 2.4 and the Supporting Information) being around $|C_Q| \sim 20$ MHz which is in the expected range. In order to understand and illustrate the impact of C_Q onto the line width of the magic angle spinning ^{35}Cl NMR spectrum, SIMPSON simulations^[24] were performed by varying $|C_Q|$ from 32 to 0.5 MHz (see inset of Figure 4a). The line width of 3.5 ppm of the experimental single ^{35}Cl resonance implies that the quadrupolar interaction is scaled by a spectral order parameter to an effective value. Due to common in-

homogenous broadening in the range of 1–2 ppm, only limits can be estimated: $\langle S \rangle < 1/40$ providing $\langle C_Q \rangle \approx \langle S \rangle |C_Q| < 0.5$ MHz. This is supported by DFT results which indicate large B-site displacements correlating with chloride diffusion (see below). Also, such notable EFG averaging seems to be due to effects caused by In³⁺ substitution and Sn vacancy creation leading to unusual structural variations. It indicates that a relaxation order parameter S^2 for $^{35}\text{Cl}-T_1$ has to be considered depending on ion hopping and phonon modes (strongest: Sn-Cl stretching),^[25] i.e., cannot be simply separated: $S^2 \neq S_{\text{hopp}}^2 S_{\text{ph}}^2$. With such sufficiently correlated averaged EFGs, basic ^{35}Cl NMR 1D MAS spectra are directly recordable, in the case of CSIC. The obtained chemical shift of the single resonance of around 110(1) ppm (156 ppm – 46 ppm = 110 ppm, referenced according to IUPAC vs powdered NaCl) agrees with the general trend of decreasing chemical shift with a reduced EFG, e.g., for CsCl with $|C_Q| < 10$ kHz, a chemical shift $\delta_{\text{iso}} = 114(1)$ ppm is reported.^[23]

Basic longitudinal relaxation measurements were carried out at RT yielding a value of 12(6) s (Figure 4b). In order to gain insight into the T_1 outcome, one has to take the relaxation order parameter S^2 into account (see the Supporting Information): $T_1 \approx \frac{10}{S^2 C_Q^2} \frac{1}{\tau_{\text{hopp}}} = \frac{10}{\langle C_Q \rangle^2} \frac{1}{\tau_{\text{hopp}}}$, with the average NMR-based chloride hopping time τ_{hopp} . Knowing the ionic conductivity, $\sigma = \frac{e^2 N_v}{kT} D = 3.45 \times 10^{-2} \text{ S m}^{-1}$ with k (Boltzmann constant), T (temperature in Kelvin), N_v (number of ions per unit cell volume: $3/172 \text{ \AA}^3$), it is possible to extract the diffusion coefficient: $D = 3.2 \times 10^{-13} \text{ m}^2 \text{ s}^{-1} = \langle x^2 \rangle / (2n\tau_{\text{diff}})$. Since the system persists 3D-processes with $n = 3$ and theoretical hopping distance of $\sqrt{\langle x^2 \rangle} \approx 1.6 \dots 3.97 \text{ \AA}$, the overall diffusion time can be estimated being $\tau_{\text{diff}} \approx (1.4 \dots 8.3) \times 10^{-8} \text{ s}$. This value range originates from impedance spectroscopy data and is depending on the dominating Cl^- hopping distance. It evidently may vary with respect to the treatment of the material, e.g., heating. This range can be considered an upper limit for an NMR-based mean hopping time that it follows for the relaxation order parameter (see the Supporting Information): $S^2 > 2.5 \times 10^{-8}$.

Taking into consideration such a high degree of crystal field variation, most of the time and within the major part of the material, chloride ions have no direct paramagnetic interaction, thus giving rise to the diamagnetically dominated ^{35}Cl NMR signal.

However, unpaired electron contributions exist nearby the chloride ions, probably during the short chloride vacancy jumping process, providing weak EPR signal contributions (Figure 4c). Recording the paramagnetic broadened ^{119}Sn NMR 1D MAS spectrum (inset of Figure 4c), the unbalanced nature within vicinity of Sn has been revealed. For indium, this has not become clear so far. But in the presence of In^{2+} , an unpaired electron contribution is supposed to exist (electron configuration $[\text{Kr}] 4d10 5s1$). Both couplings of the local electron spin distribution to the nearby nuclear spins of tin— ^{115}Sn , ^{117}Sn , ^{119}Sn : related to their abundance ratio of 4:89:100 (all isotopes with spin 1/2)—and indium— ^{113}In and ^{115}In : with ratio 4:100 (both with spin 9/2)—were not directly detectable by EPR (exceedingly large hyperfine couplings $|A_{\text{Sn}}| > 40 \text{ GHz}$ and $|A_{\text{In}}| > 20 \text{ GHz}$ compared to the 9.7 GHz X-band technology).^[26]

2.4. Density Functional Theory

In a first step, the cubic CsSnCl_3 and the In-doped supercells were investigated with respect to their monoclinic counterparts (see the Experimental Section and Tables S3–S5, Supporting Information for structural details). Interestingly, in the case of the pristine CSC structure, the cubic phase is only metastable, meaning that the monoclinic phase is energetically favored (by 5 meV at^{-1}). For the doped sample on the other hand, In is able to stabilize the cubic phase. In fact, for the two investigated compositions, $\text{CsSn}_{0.875}\text{In}_{0.125}\text{Cl}_3$ and $\text{CsSn}_{0.93755}\text{In}_{0.0625}\text{Cl}_3$, the cubic phase is slightly more stable by ≈ 7 and $\approx 0.2 \text{ meV at}^{-1}$. While these differences are indeed very small, the stabilizing impact of an increasing In content still becomes evident (Table S5, Supporting Information). Interestingly, if the In-doping in $\text{CsSn}_{0.93755}\text{In}_{0.0625}\text{Cl}_3$ is compensated by a vacancy on the Sn site neighboring the In site, the stabilization of the cubic phase is significantly increased, now amounting to $\approx 13 \text{ meV at}^{-1}$. Thus, both In substitution and charge compensating vacancies at the Sn sites have a stabilizing effect on the cubic structure.

For comparison with NMR measurements, the EFG was determined for the undoped and In-doped cubic CSC (Tables S6–S9, Supporting Information). In this context, it has to be noted that for not fully charge balanced model systems, localized magnetic moments have been observed on In or Sn, which may hold as an explanation for the observed EPR signal (see above).

To investigate the impact of In doping on the ion mobility, the kinetics of the material was determined by investigating the Cl-ion diffusion in a large $3 \times 3 \times 3$ supercell of undoped cubic CSC and In-doped cubic $\text{CsSn}_{0.9815}\text{In}_{0.0185}\text{Cl}_3$ (see the Experimental Section). For this purpose, both an interstitial-based knock on mechanism and vacancy-mediated Cl^- diffusion have been investigated by the nudged elastic band method (see the Experimental Section). For the undoped sample, the interstitial mechanism showed a barrier of $\approx 0.48 \text{ eV}$ (Figure S9, Supporting Information), whereas the barrier for a Cl ion moving to a neighboring vacancy was observed to be as low as $\approx 0.2 \text{ eV}$, which agrees with the value reported in literature (Figure 4f). From these findings, the vacancy mechanism was concluded to be the dominant diffusion process, and therefore only this process was further investigated for the case of In doping. Interestingly, the doped structure shows an even lower diffusion barrier for Cl ions neighboring the In site, which seems to be triggered by increased displacements of the In atoms during a diffusion event. Here, an extremely low barrier of less than 0.1 eV is found. Moreover, it has to be noted that the structures generally show a high structural flexibility during the diffusion process. This means that the presence of a Cl vacancy results in significant distortions of the SnCl_6 (InCl_6) octahedra that propagate throughout the structures. These distortions do not only result in displacements of Cl ions but also affect the In/Sn sites in the vicinity of the Cl vacancy, as indicated in Figure 4d,e. In the case of the In-doped sample, large In ($\approx 2 \text{ \AA}$) and Sn ($\approx 0.6 \text{ \AA}$) displacements are observed close to the diffusing Cl ion, while in the undoped sample, further increased Sn displacements are present. The fact that apart from the diffusing Cl ion, other atoms are easily displaced during a diffusion event results in a shallow but complex potential energy landscape. Despite the generally low diffusion barriers, the positive impact of the In^{3+} substitution on the diffusion barrier in the vicinity of the In atom is quite evident. On the other hand, if a diffusion event occurs further away from the In dopant, the diffusion barrier is essentially not affected. Finally, a vacancy on a Sn site close to the diffusing chloride ion results in an increase of the diffusion barrier to 0.31 eV . Thus, the In^{3+} doping results in a stabilization of the cubic phase, while the impact on the diffusion is more difficult to assess. However, due to the small In/vacancy content on the Sn sites, it seems reasonable that the diffusion properties are dominated by the barriers of the undoped compound. In general, it has to be emphasized that the impact of structural flexibility of the In/SnCl_6 octahedra, observed also by NMR and EPR (envisaged by spectral and relaxation order parameters $\langle S \rangle$ and S^2), can be understood as lying the origin of the good Cl^- diffusion in this material.

2.5. Electrochemical Performance of ASSB

Among the important parameters, that determine the efficiency of an ASSB, sufficient percolation of CAM by the SE is crucial in maximizing the electrochemical performance of the

electrodes used. The ionic and electronic conduction/percolation within a cathode composite and the ability to overcome the volume changes are compulsory requirement of a CAM. Since various CAMs exhibit different degrees of volume expansion/contraction, exploration of cathode materials with negligible volume changes during Cl^- extraction/insertion is needed. In addition, compressive stress on the SE and electrodes would supplement the contact/ionic percolation and minimize the volume expansion.

Depending on the nature and loading of the CAM, ionic/electronic conductivity might vary substantially. In this study, we have tested two different CAMs, (namely, WOCl_4 and VCl_3), both of which undergo conversion-type reactions. Details of ASSB assembly are provided in the Experimental Section (XRD and SEM results of the cathode composite are compiled in Figures S5–S7, Supporting Information). A schematic representation of the ASSB system with Li/SE/cathode composite is shown in Figure 5a. A cross-sectional view of the ASSB is obtained using focused ion beam (FIB-SEM) technique that clearly visualizes the separation of cathode composite layer and electrolyte layer in Figure 5b. The cathode composite layer was nearly 20 μm thick, where CAM (orange) and SE particles (blue) could be seen to be distributed between carbon particles. Figure 5c shows the SEM image of an individual CAM particle in the cross-sectional view. The optical image of bare electrolyte pellet and assembled ASSB is shown in Figure 5d.

The as-assembled ASSB had an open circuit voltage (OCV) of 2.5 V, which is similar to the liquid electrolyte cell containing WOCl_4/Li electrodes.^[24] Electrochemical investigation was initiated by subjecting the ASSB to impedance spectroscopy at RT. This is expected to provide an insight on how well the electrodes were interfaced with SE and if at all, the SE was chemically stable with respect to the electrodes.

Due to the scarcity of EIS studies on anionic ASSBs in literature, we had to apply suitable concepts analogous to solid-state lithium-metal batteries. In order to roughly deconvolute the impedance contributions from the anode and the cathode in full cell arrangements, we first constructed Li|SE|Li (Figure S10, Supporting Information), CAM|SE|CAM symmetric cells (Figures S11 and S12, Supporting Information) and measured their impedance spectra (details are given in the Supporting Information). The Nyquist plots of the WOCl_4/Li full-cell (recorded 1 h after cell construction) were fitted with an equivalent circuit model consisting of a series combination of four parallel R||CPE components (Figure 5e). The R||CPE component corresponding to the partial semicircle in the high-frequency region (≈ 1 MHz) was attributed to the transport of chloride ions through the SE, while the one at ≈ 2.5 kHz was assigned to the solid electrolyte interphase (SEI) formed at the interface between the solid electrolyte and the LMA as it was in alignment with the processes identified in the Li symmetric cell. However, the R||CPE component corresponding to the anode side charge transfer resistance at ≈ 50 Hz (as per the Li|SE|Li data) was difficult to identify in the full-cell since it was completely hidden by the disproportionately large semi-circle corresponding to the cathode side (560 k Ω).

To obtain insight in the involved redox reactions of the all-solid-state cell, cyclic voltammetry (CV) was carried out in the voltage range of 0.5–3.9 V at RT, with a scan rate of 2 mV s^{-1} (Figure 5f). During the first cathodic scan, a reduction peak was observed be-

tween 1.5 and 0.5 V, followed by a pronounced oxidation peak at ≈ 2.0 V and a second broader oxidation peak at around 2.8 V. In the subsequent cycles, the redox peaks underwent a slight negative shift accompanied by a reduction in peak currents. The decrement of the peak currents could be due to the irreversible charge transfer between the electrodes, or undesired chemical side reactions between SE and electrodes. That implies a possible increase in SE-electrode interphase resistances. The quasi-reversible redox reactions as indicated by CV measurements have been further investigated by electrochemical cycling as discussed below.

Galvanostatic cycling results of the WOCl_4 CAM displayed similar redox features as indicated by the CV (Figure 5g). After the initial potential drop to 1.7 V from 2.5 V (OCV), a sloping region was observed between 1.6 and 0.8 V during the discharge. From 0.8 to 0.5 V, further de-chlorination processes continued, accounting for a first discharge capacity of 156 mAh g^{-1} , corresponding to $\approx 50\%$ of the theoretical capacity of WOCl_4 (313 mAh g^{-1}). The first charge curve featured two plateau regions, at around 2.7 and 3.6 V. Overall, the first cycle yielded a reversible capacity of 108 mAh g^{-1} . WOCl_4 suffers severe capacity fading over 20 cycles with ≈ 82 mAh g^{-1} reversible capacity (Figure 5h). From previous work on WOCl_4 , it is known that the material undergoes a conversion-type reaction.^[24] The capacity fading over the cycle number could result from the volume changes at the cathode/anode sides, which weakens the electrical contact between the CAM, SE, and conductive carbon, thus increasing the charge transfer resistance.^[25] An XPS investigation of the cycled LMA shows metal chloride formation (Figure S13, Supporting Information). During battery cycling, the CSIC/cathode interface is predicted to decompose via chemical mixing, if exchange of ions between SE and cathode is energetically favorable and not kinetically hindered. Similar behavior has often been observed in LIB ASSBs, e.g., in $\text{LiCoO}_2/\text{Li}_2\text{S-P}_2\text{S}_5$.^[8] This likely results in an increase in resistance at the cathode side of the cell.

2.6. Humidity Tolerance and Air Processability

Most sulfide-based lithium conducting SEs ($\text{Li}_6\text{PS}_5\text{Cl}$ (LPSC),^[26] Thio-LISICON $\text{Li}_{10}\text{GeP}_2\text{S}_{12}$ ^[27]) are sensitive to air (oxygen and H_2O), which limits their application despite possessing high ionic conductivities at RT and favorable mechanical properties.^[28] Due to easy substitution of S^{2-} ions by O^{2-} from moisture, they tend to release H_2S gas (weak Li–S bonding), upon exposure to moist air.^[29] In comparison to sulfide-based SEs, halide-based SEs seem to have better air stability, as for instance observed for Li_3InCl_6 .^[30] To evaluate the humidity tolerance of CSIC, we considered two samples: pristine CSIC and heat-treated CSIC (2 h at 140 $^\circ\text{C}$ in vacuum/CSIC-HT). The heat treatment was applied, as it was expected to have a stabilizing effect on the lattice due to release of strain and the grain boundary ordering as well.^[17] In fact, this is reflected in slightly enhanced conductivity (3.45×10^{-4} S cm^{-1}), which is higher than the value of CSIC and CSC-HT. Both samples were exposed to ambient air, with a measured relative humidity (RH) level of $\approx 50\%$, for 3 h each. The X-ray diffractogram of CSIC HT indicated no structural changes (Figure 6a). While, a minute change in the ionic conductivity with a decrease to 2.84×10^{-4} S cm^{-1} , indicating overall an

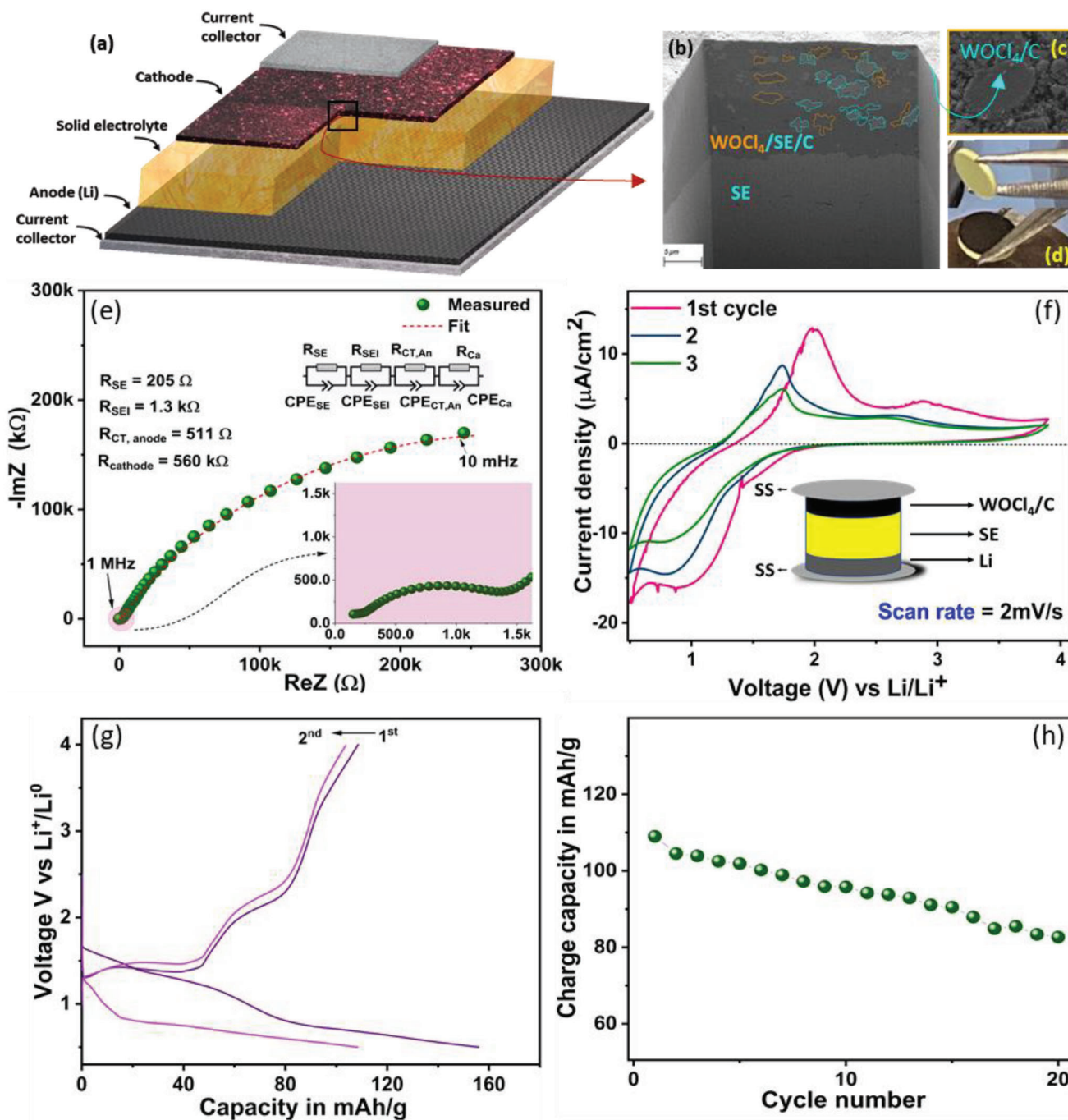


Figure 5. a) Schematic representation of an all-solid-state chloride-ion battery, b) SEM cross-sectional image of an ASSB, from cathode/SE side; the layers of $\text{WOCl}_4/\text{C}/\text{CSiC}$ and CSiC can be seen, c) CAM particle in the composite, d) optical images of electrolyte and cathode side of the pellet, e) Nyquist plot of all solid-state chloride-ion battery at RT; inset: respective equivalent circuit used for the spectra, f) cyclic voltammetry of all-solid-state chloride-ion battery, $\text{Li}/\text{CsSn}_{0.9}\text{In}_{0.067}\text{Cl}_3/\text{cathode}$ composite, $\nu = 2 \text{ mV s}^{-1}$, g) galvanostatic discharge–charge curves of ASSB, $\text{Li}/\text{CsSn}_{0.9}\text{In}_{0.067}\text{Cl}_3/\text{cathode}$ composite. h) Capacity versus cycle number plot of ASSB.

insignificant humidity intake in CSiC-HT (Figure 6b). This fact ascertains that even at a very high RH level of 50%, CSiC-HT retains its intrinsically conducting cubic phase, which is a significant advancement achieved compared to the metastable CsSnCl_3 (in inert atmosphere). The respective air exposure data of CSiC are provided in Figure S14a,b in the Supporting Information.

2.6.1. Regeneration Test

Both CSiC and CSiC HT samples showed excellent structural regeneration abilities after a high-level humidity exposure to 95% RH in ambient air. Cubic CSiC changed to insulating, pure monoclinic phase ($1.25 \times 10^{-9} \text{ S cm}^{-1}$), while CSiC HT

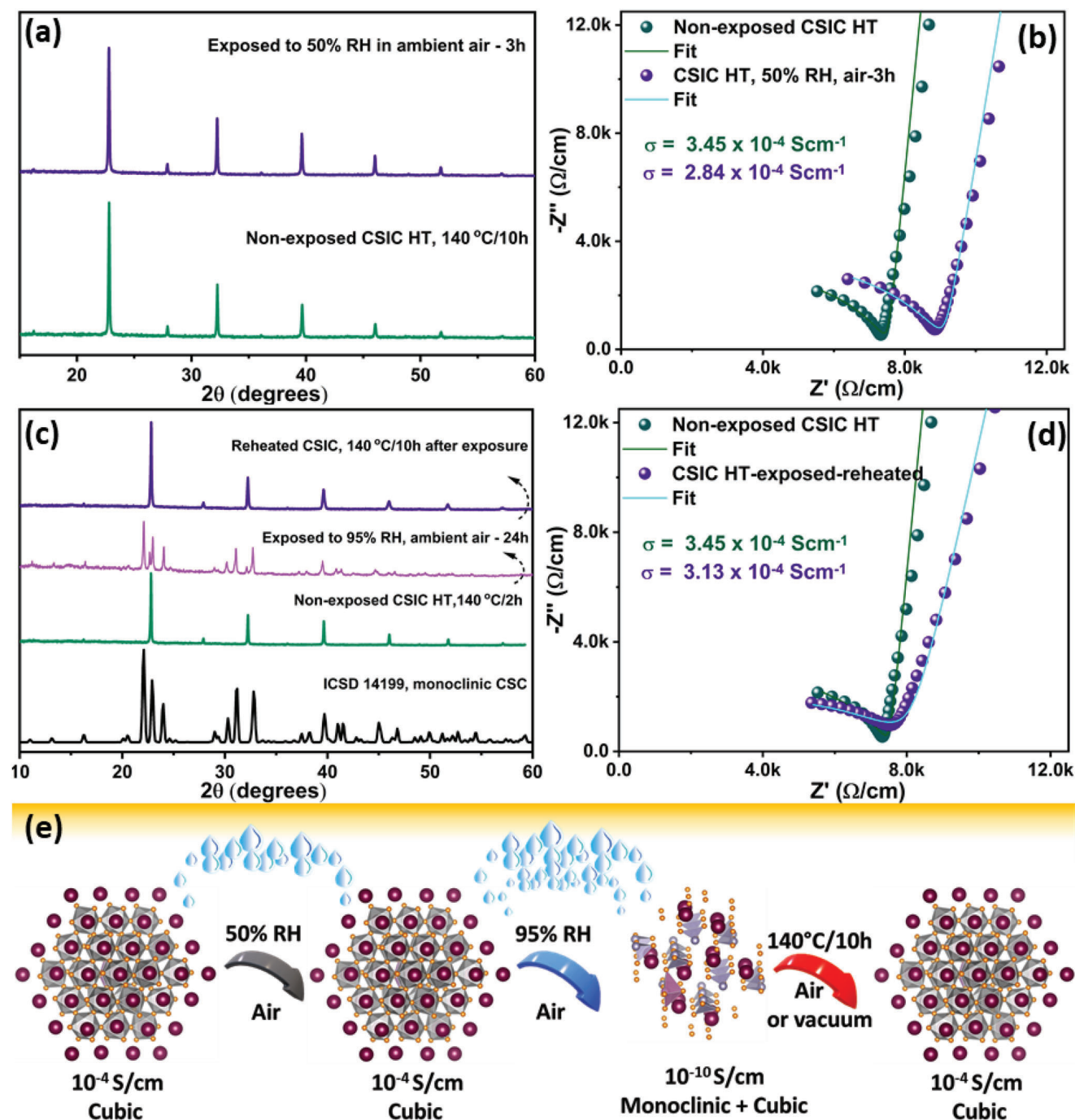


Figure 6. Air/humidity tolerance and regeneration tests of CSIC-HT: a) XRD patterns after exposure to air with $\approx 50\%$ RH level, b) corresponding EIS spectra showing their derived ionic conductivities. c) XRD patterns after exposure to air with $\approx 95\%$ RH level and followed reheating, d) corresponding EIS spectra showing their derived ionic conductivities. The EIS spectrum of monoclinic phases is given in Figure S15 in the Supporting Information for comparison. e) Schematic representation of structure revival abilities of $\text{CsSn}_0.9\text{In}_{0.067}\text{Cl}_3$ during air exposure.

transformed to a monoclinic-cubic, mixed phase ($7.11 \times 10^{-10} \text{ S cm}^{-1}$, Figure S15, Supporting Information), both of which could be restored to pristine conductive phases, by a heat treatment of 140°C for 10 h in air or vacuum (Figure 6c,d and Figure S14c,d, Supporting Information). This is a sustainable feature of this material that air exposure does not lead to decomposition and

causes chloride loss from the structure, which is one of the challenges in commercial sulfide/halide-based solid lithium conductors, e.g., LPSC,^[31] which increases their processability cost during the commercial cell development. For comparison, a similar air exposure test was performed with LPSC and the results show an irreversible decomposition to new phases after moist air

exposure, which also cannot be recovered by heating (Figure S16, Supporting Information).

2.7. Stability against the Metal Anodes

Designing a practically applicable SE is challenging mainly because of the critical contact circumstances at cathode and anode sides. Poor solid-to-solid contact limits the capacity utilization and delivery of the expected performance. The establishment of desired electrochemical and chemical neighboring between SE and electrodes plays a critical role in achieving a good long-term cyclability of the battery. In most cases, SEs tend to reduce in contact with metal anode and oxidize upon reaction with high-voltage cathodes.^[32]

The activity of halide-based electrolytes with lithium has been well-studied in lithium metal-based ASSBs,^[30] but, their reactivity with relatively hard metals like magnesium and calcium is unknown. To check the electro-/chemical stability of CSIC with metal anodes and its feasibility as an RT SE, we have extended the electrochemical experiments on another CAM VCl_3 and studied its electrochemical stability versus four different metal anodes, namely, Li, Li–In, Mg, and Ca. In the first step, the temporal evolution of full-cell impedances was measured (on an hourly basis up to 6 h under resting condition) to understand the chemical stability of metal with SE, and CV experiments were carried out to demonstrate the ionic transfer through the solid interphases, i.e., between electrodes and SE.

2.7.1. With Lithium

Figure 7a shows the impedance spectra of the $VCl_3/SE/Li$ ASSB (OCV of 2.24 V) as a function of time. The analysis of these spectra revealed a high-frequency semi-circle with a characteristic frequency of around 1 MHz which could be attributed to the SE impedance. The full-cell with Li anode showed another semi-circle with a characteristic frequency of 2.5 kHz associated with the anode side. The size of this semi-circle grew from 580 Ω in the first hour to 1338 Ω in the sixth hour.

The first five CV cycles of the corresponding ASSB (**Figure 8a** and **Figure S16**, Supporting Information) reveal redox activity in the voltage window of 0.6–2.5 V. During the cathodic scan (dechlorination), a single reduction peak was located near 1.2 V, which propagates until 0.6 V in the later cycles. In the first anodic scan, two oxidation peaks were observed near 1.5 and 1.6 V. These redox features are most probably related to the interconversion of vanadium redox, V^{3+}/V^{2+} . It is important to note that from the second cycle onward, the oxidation peak was negatively shifted to 1.44 V and the peak currents reduced, which could be due to the chemical instability of cathode/anode with SE, as well as the connected volume changes. The cell performance could also be affected by the type of the formed interphase (e.g., mixed conductive interphase, MCI) and its nature of ionic/electronic conductivity. If the SE is reactive toward metal anode, the new interphase could contain mixture of Cs^+ , Sn^{2+} , In^{3+} , and Cl^- ions, with the LMA/or other metals used as anodes in this study.^[33] The temporal increase of anodic impedance (**Figure 7a**) and a color change at the interphase of Li-CSIC (**Figure S18**, Supporting Information)

corroborates the idea of new SEI formation in the anode side. These aspects were further studied by XPS and will be discussed later in more detail.

2.7.2. With Lithium–Indium Alloy

Figure 7b shows the impedance spectra of an ASSB comprising $VCl_3/SE/Li-In$ (OCV = 1.57 V). The full-cell showed a semi-circle with a characteristic frequency of around 1250 Hz which gradually increased from 2705 Ω in the first hour up to 4312 Ω in the sixth hour. It may be noted that the deconvolution of the contributions from SEI and charge transfer resistance of the anode side in the full-cells with Li and Li–In anodes were not feasible with the two-electrode cell set-up used in this study and would require three-electrode impedance measurements which is out of the scope of this study.

The CVs of ASSB with Li–In alloy anode are given in **Figure 8b**. The first reduction peak, at 0.7 V was followed by a sharp anodic peak located at 1.18 V. Ideally, due to the change in reference electrode, the peak positions would negatively shift by 0.63 V in comparison to the previously discussed LMA. The observed shift of the anodic peak from 1.6 V (vs Li^+/Li) to 1.18 V versus Li–In alloy agrees thus rather well with the change of reference electrode. A shift of the anodic peak to higher potentials (1.5 V) was noted in later cycles, together with a reduction in the peak current. This could be due to the overpotential from interfacial reaction products at either side of the electrodes.

2.7.3. With Magnesium

Figure 7c shows the impedance spectra of ASSB with $VCl_3/SE/Mg$ (OCV = 1.4 V). The spectra of the full-cell with Mg anode consisted of two semi-circles in the mid-frequency region with characteristic frequencies of 30 and 2 Hz that could be attributed to the anode side. Mg being a rather stiff metal cannot achieve a good contact with the SE, as in the case of the softer Li metal and Li–In alloy. This could result in a major contribution to the increased interfacial resistance, along with possible resistance contributions from SE-Mg/SE-cathode interphases. The anode side resistance grows over 150 k Ω in 6 h. The first CV cycle (**Figure 8c**) features several distinct redox peaks, with the cathodic peak being more like a decremental wave. The anodic peak was observed at 1.12 V, i.e., with a negative shift of 0.5 V versus Li/Li^+ , which to a large extent can be attributed to the difference in reduction potential of the magnesium electrode. In the following cycles, redox features were stable, indicating a stabilized interphase formation in comparison to Li and Li–In anodes. The respective optical images of the Mg metal and SE after cycling (**Figure S19a,b**, Supporting Information) indicate gray-colored regions, confirming the new interphase formation whose composition will be discussed in the following sections based on the XPS results.

2.7.4. With Calcium

The impedance of the $VCl_3|SE|Ca$ cell (OCV = 1.24 V) showed a different behavior compared to the cells with other anode materials (**Figure 7d**). It consisted of two semi-circular features in

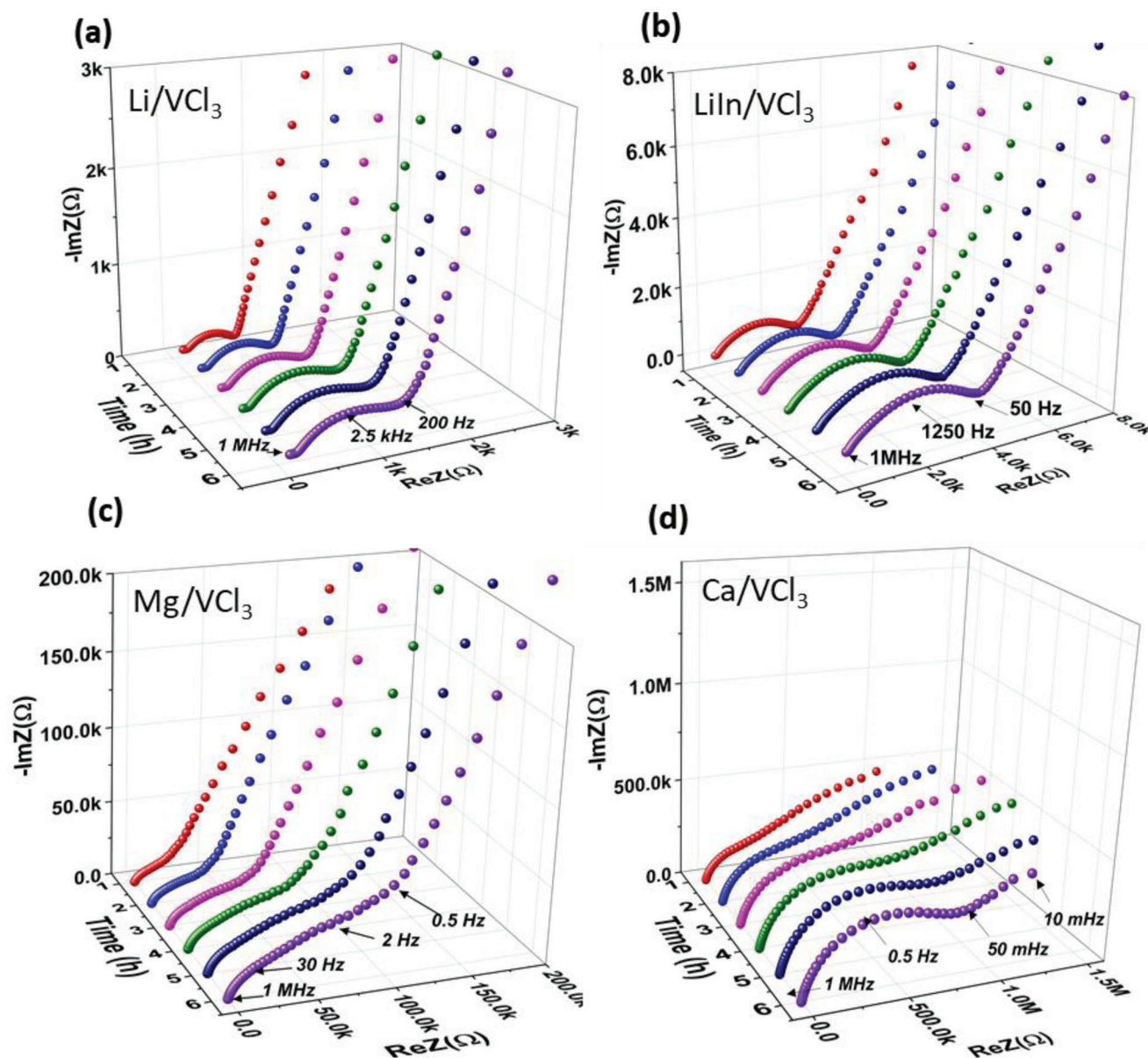


Figure 7. Stability of CSIC against different anodes in ASSBs containing VCl_3 as CAM: Time-dependent impedance spectra with a) Li, b) Li–In, c) Mg, and d) Ca anodes, at RT.

the lower middle and low-frequency regions. The circle in the lower mid-frequency region with a characteristic frequency of 0.5 Hz could be attributed to the SEI resistance and the partial semi-circle in the low-frequency region had a characteristic frequency lower than 10 mHz. However, we can distinguish this low-frequency semi-circle from that of the cathode side on the basis of their temporal evolution behavior. The impedance of the low-frequency partial semi-circle in the $VCl_3/SE/Ca$ cell initially increases during the first 4 h, followed by a decreasing trend. This second circle therefore could be attributed to the charge transfer impedance on the Ca anode side. The anode side impedance shows extremely high values of more than 1 M Ω . The high interfacial anodic impedance could be attributed to the stiffness of Ca metal and resulting contact issues with the SE similar to the

case of the Mg anode. The CV of the corresponding cell is shown in Figure 8d. The distinct cathodic peak was located at ≈ 0.63 V. The anodic peak was observed at ≈ 1.09 V, which is 0.5 V lower than that of Li cell and can mostly be associated with a high overpotential at the anode side. With cycling, the peaks seem to be well resolved and reproducible, after the 11th cycle, indicative of a favorable/stabilized interphase composition, although peak currents are rather low, due to sluggish charge transfer kinetics. The respective optical images of the Ca metal and SE after cycling (Figure S19c,d, Supporting Information) indicate a color change, confirming the formation of a new interphase which will be investigated by XPS (see below).

In the next step, the chemical species at different anodes (Li, Li–In, Mg or Ca) after cycling were investigated by XPS

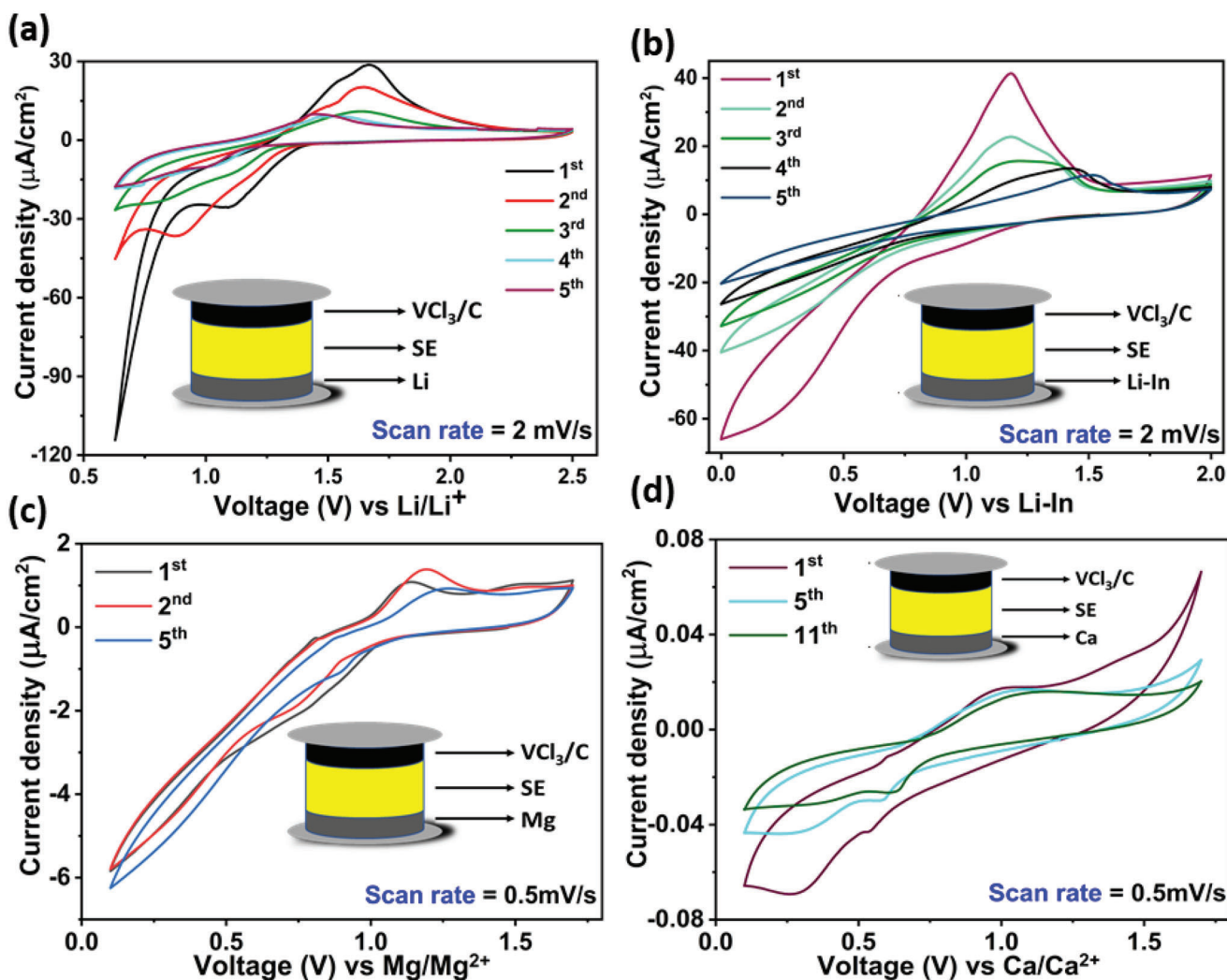


Figure 8. Charge transfer capabilities of SE with different metallic anodes, at RT: a) Li, CV between 0.6 and 2.5 V and $\nu = 2 \text{ mV s}^{-1}$, b) Li-In, CV between 0.0 and 2.0 V and $\nu = 2 \text{ mV s}^{-1}$, c) Mg, CV between 0.1 and 1.7 V and $\nu = 0.5 \text{ mV s}^{-1}$ and d) Ca, CV between 0.1 and 1.7 V and $\nu = 0.5 \text{ mV s}^{-1}$.

determine the interfacial SEI products resulting from the electrochemical reactions with the SE. The corresponding XPS detail spectra are collected in **Figure 9**. In the Li 1s spectrum of the Li anode (Figure 9a), a single peak at 56.3 eV is detected, which can be assigned to LiCl (or other Li salts with a similarly electronegative anion). After sputtering, a new peak emerged at lower binding energy (at 55.1 eV) that is most probably caused by the presence of Li_2O in deeper layers, which is corroborated by the appearance of a prominent new peak at 528.7 eV in the O 1s detail spectrum in Figure S20i in the Supporting Information.^[34] For the Li-In anode (Figure 9b), the Li 1s peak is relatively weak both before and after sputtering, indicating a relatively thick layer of electrolyte residues and/or other deposits on the surface. The peak is detected at 55.9 eV, indicating that various Li species may be involved here. Three peaks are detected in the Mg 2p spectrum of the Mg anode (Figure 9c); the first one at the lowest BE (48.7 eV) can be assigned to metallic Mg, the last one at the highest BE (51.5 eV) to MgCl_2 , whereas the feature in between (at ≈ 50 –50.5 eV) is due to other Mg salt species, e.g., oxides (a corre-

sponding O 1s peak is detected at 529.8 eV in Figure S20k, Supporting Information). While the peak of metallic Mg is rather small initially, it grows considerably after the sputter treatment indicating a rather thin deposit layer on the surface of the Mg anode. Conversely, the MgCl_2 feature loses significantly in intensity by the sputter step. Finally, before sputtering, the Ca 2p spectrum of the Ca anode (Figure 9d) is dominated by a peak doublet (at 348.1/351.5 eV), which can be assigned to CaCl_2 .^[35] Another, relatively small, peak doublet due to CaO and other oxidized Ca species is also detected at slightly lower BE (347.1/350.5 eV). After sputtering, the intensity of the CaCl_2 peak doublet decreases, while the intensity of the CaO feature grows. In addition, a new peak doublet at even lower BE (345.8/349.3 eV) can be detected after sputtering which is due to metallic Ca.^[35]

For all four metal-SE surfaces, electrolyte components could also be detected by XPS. The detail spectra in the Cl 2p region (Figure 9e–h) showed in most cases two peak doublets, which can be assigned to the electrolyte (Cl $2p_{3/2}$ peak at 198.3 eV) and the respective metal chlorides (i.e., LiCl, MgCl_2 , or CaCl_2 ; Cl $2p_{3/2}$

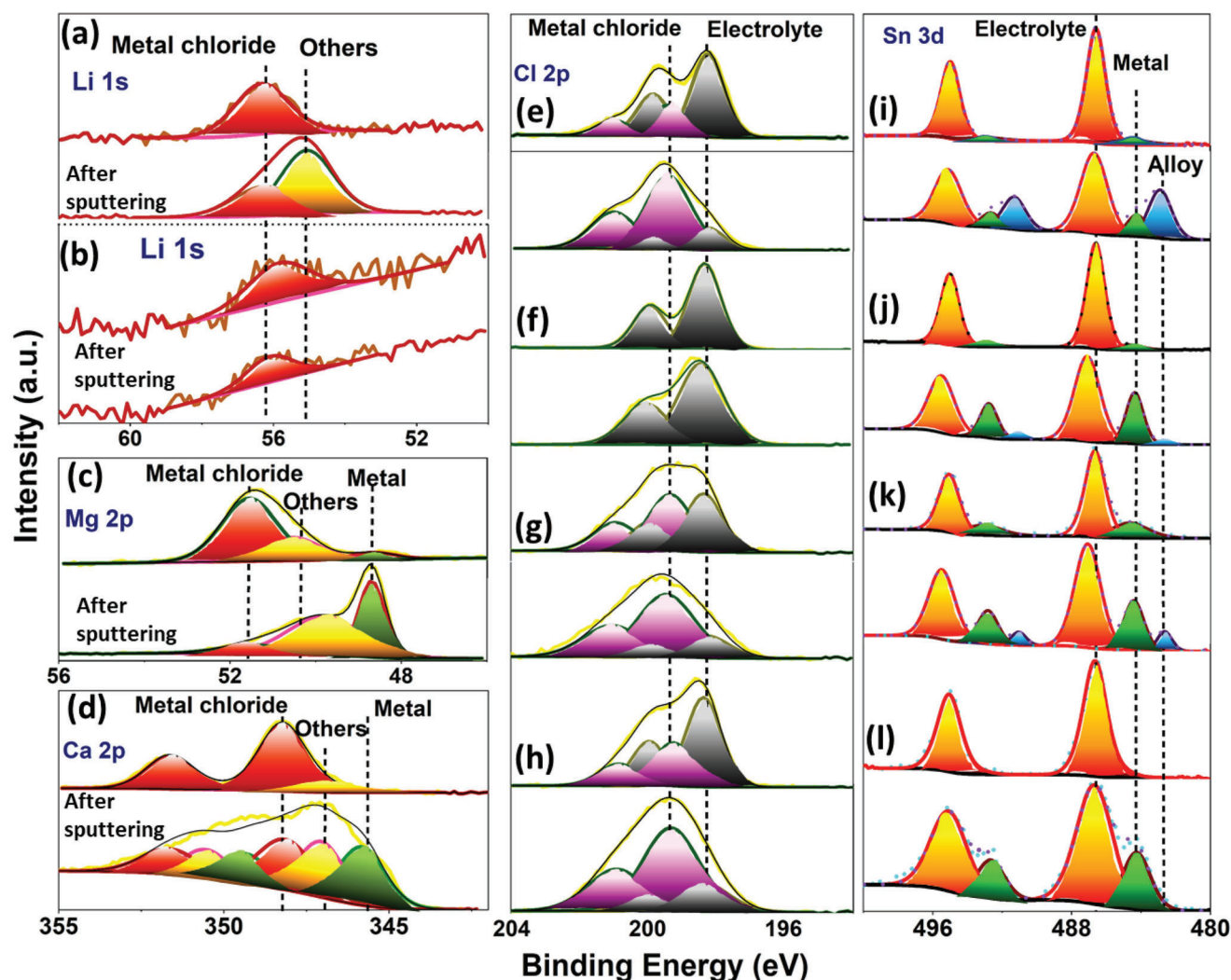


Figure 9. XPS analysis of cycled metal anodes before and after Ar^+ ion sputtering for 5 min; a,e,i) Li 1s, Cl 2p, and Sn 3d spectra from Li anode; b,f,j) Li 1s, Cl 2p, and Sn 3d spectra from Li–In anode, c,g,k) Mg 2p, Cl 2p, and Sn 3d spectra from Mg anode, and d,h,l) Ca 2p, Cl 2p, and Sn 3d spectra from Ca anode, collected from ASSB cells used for the CVs in Figure 8.

peak at 199.2–199.4 eV). In the case of the Li–In electrode, only the electrolyte signal was detected due to the relatively thick cover layer on the surface. For the other three electrodes (Li, Mg, and Ca), a reduction of the electrolyte signal and growth of the metal chloride signal was observed upon sputtering. In the Sn 3d region of the spectra (Figure 9i–l), small contributions from reduced (metallic) Sn could be detected already for the un-sputtered Li, Li–In, and Mg samples (peak doublet at 484.7/493.1 eV) besides the dominant peak doublet of the Sn^{2+} ions in the electrolyte (486.7/485.1 eV). After sputtering, the signal of metallic Sn increased for all four metal anodes, while the formation of a new peak doublet at even lower BE (Sn $3d_{5/2}$ peak at ≈ 483 eV) indicates the formation of alloys with Li and Mg. Before sputtering, Cs was found in all cases in oxidized form (Cs^+) as expected from the electrolyte, with a Cs $3d_{5/2}$ peak binding energy of 724.3 eV (Figure S20a–d, Supporting Information). Interestingly, the reduction of a part of the Cs atoms to metallic state was observed in the measurements of the Li and Ca samples after sputtering (Cs

$3d_{5/2}$ peak at 725.9 eV).^[36] In^{3+} remained in the original chemical state, when in contact with Li, Li–In, or Ca (In $3d_{5/2}$ peak at 445.3 eV) while a small additional signal of metallic (or alloyed) In was detected in the measurement of the Mg surface (In $3d_{5/2}$ peak at 442.6 eV). After sputtering, except for Ca, other three metals witnessed a growth of the intensity of the feature of this metallic/alloyed species (Figure S20e–h, Supporting Information).

In general, among the possibilities to form different anodic interphases, such as i) a thermodynamically stable interface, ii) a stable SEI with negligible electronic conductivity, iii) a mixed ionic–electronic conducting interphase (MCI); (i) and (ii) correspond to favorable interphases. On correlating the XPS results, the Ca surface was found to be less reactive toward Cs^+ , Sn^{2+} , and In^{3+} cations, while in the case of the Li and Li–In surfaces some Sn^{2+} ions were reduced (possible formation of Li–Sn alloy) and $\text{Cs}^+/\text{In}^{3+}$ ions remain unchanged. On the Mg surface, Cs^+ ions remain intact, while Sn^{2+} and In^{3+} ions were partially reduced to the metallic state (possible formation of Mg–In/Sn alloy). As

reduced/metallic, electrolyte elements could form an alloy with the corresponding anodes, the possibility of forming MCI cannot be excluded for the investigated metals except for the case of calcium.

3. Conclusion

A fast chloride-ion conducting, halide perovskite ($\text{CsSn}_{0.9}\text{In}_{0.067}\text{Cl}_3$) was prepared by annealing free, quick mechanical milling, which displays an RT ionic conductivity of $3.2 \times 10^{-4} \text{ S cm}^{-1}$. The impedance spectroscopy, DFT, solid-state ^{35}Cl NMR, and EPR studies in conjugation reveal that the high Cl^- ionic mobility originates in a high dynamical flexibility of the structural building blocks, Sn/InCl_6 octahedra. The vacancy-mediated Cl^- ion diffusion is accompanied by coordinated Sn/In site displacements, which promote the fast ion conduction. With favoring properties as a SE, the investigation of CSIC extends the range of available electrode materials from metal oxides, sulfides, polyanionic compounds to chlorides, as demonstrated by the respective ASSB performances with WOCl_4 and VCl_3 electrodes. Moreover, this work addresses the existing hurdle of electrode solubility in liquid electrolyte-based CIBs. The stabilized $\text{CsSn}_{0.9}\text{In}_{0.067}\text{Cl}_3$ demonstrated an excellent humidity tolerance (up to 50% RH) in ambient air and structure revival capabilities without compromising its ionic conductivity. The structural regeneration property of this material could lead to futuristic developments of commercial air processable SEs, which is of great significance for commercial battery cell production. The comparative investigation of the charge transfer ability of the electrolyte with Li, Li–In, Mg, and Ca anodes revealed chloride-rich anodic interphases and while a quasi-reversible charge transfer was evident even with hard-metallic anodes like Mg and Ca. This discovery of halide perovskite ionic conductor paves the way for the exploration of untapped classes of metal chloride materials and the development of air processable SEs for advanced battery technologies.

4. Experimental Section

Synthesis of Electrolyte and Electrode Materials: CSC and CSIC were prepared by ball-milling stoichiometric amount of CsCl (Emsure, for analysis, Merck), InCl_3 (99.999%, Alfa Aesar), and SnCl_2 ($\geq 99.99\%$, Sigma Aldrich) powders. The milling was carried out in a Si_3N_4 ball mill jar, at 600 rpm (Fritsch Pulverisette 6) with a ball to powder mass ratio of 20:1 for 3 h in the case of CSC and 30 min for CSIC. All the precursors were dried overnight in a vacuum oven at 120°C to remove any possible moisture prior to the synthesis and were handled inside an argon-filled glove-box with both O_2 and H_2O levels < 0.1 ppm. Ball-milling procedures consisted of repetitions of a milling time of 30 min with a pause of 10 min between repetitions.

Cathode-electrolyte composite was prepared by ball-milling the active materials WOCl_4 (Aldrich) or VCl_3 (Alfa Aesar) with Super C65 conductive carbon black (Timcal) and CSIC in the weight ratio 3:1:6 at 100 rpm for 1 h. The ball to powder ratio chosen for the composite preparation was 10:1. LPSC was used as a reference-halide-based solid ion conductor and was purchased from NEI corporation.

Heat Treatment Methodology: CSC-HT was obtained by heating CSC at $140^\circ\text{C}/2$ h in vacuum, CSIC-HT was achieved by heating at $140^\circ\text{C}/2$ h in air or vacuum and cubic phase was regenerated from a humid-air-exposed CSIC by heating at 140°C for 10 h in air or vacuum.

Material Characterization: The crystal structures of the solid electrolytes (SEs) and cathode composites were investigated with XRD using

a Stadi P diffractometer (STOE & Cie) in transmission mode with $\text{Cu-K}\alpha$ radiation ($\lambda = 1.540562 \text{ \AA}$).

The morphology of the samples was visualized using field-emission SEM (FESEM, Carl-Zeiss LEO 1530 instrument) and the elemental composition was qualitatively analyzed by EDX, using a X-Max 50 detector from Oxford Instruments. The thermal characteristics of the SE were studied by DSC, with a Discovery DSC, (TA Instruments). The sample was enclosed within an aluminium pan with lid inside the argon-filled glove-box which was then crimped to prevent exposure of the sample to ambient air. During the measurement, the sample was initially cooled from 40 to -120°C and then heated to 150°C . The cooling and heating rate were both maintained at 5°C min^{-1} . Raman spectroscopy was performed with an inVia confocal Raman microscope (RENISHAW) with a 532 nm laser as the excitation light source. Laser light was focused on the sample by using a $50\times$ objective (Carl Zeiss). The spectrum acquisition time was set to 2 s and the spectral range to $50\text{--}400 \text{ cm}^{-1}$. XPS measurements were collected at a PHI 5800 MultiTechnique ESCA System (Physical Electronics) using monochromatized $\text{Al K}\alpha$ radiation (250 W , 13 kV), a detection angle of 45° , and a pass energy at the analyzer of 29.35 eV for the detail measurements. The metal anodes were transferred after the disassembly of the cells in a glove box under inert gas to the load lock of the XPS system. Spectra were acquired directly after sample transfer and after removal of the topmost surface layer by Ar^+ ion sputtering (5 min with $1 \mu\text{A}/5 \text{ kV}$, the sputter rate was $\approx 1 \text{ nm min}^{-1}$ under these conditions). The $\text{C } 1s$ peak of adventitious carbon was used for BE calibration and set to 284.8 eV . Peak fitting of the spectra was done with CasaXPS, using Gaussian–Lorentzian peak shapes and the expected values for intensity ratios and spin–orbit-splitting of the various peak doublets.^[37] NMR measurements were carried out in a 9.4 T magnetic field with a Bruker Advance III spectrometer using a double resonance 4 mm MAS probe. Direct ^{35}Cl 1D NMR spectra were recorded at 15 kHz MAS using an excitation pulse of $2 \mu\text{s}$ at a B_1 rf-field of 38.5 kHz (90° pulse length of $6.5 \mu\text{s}$ obtained with Na^{35}Cl) and a spectral-width of 10 MHz . Referencing was performed with Na^{35}Cl (s) setting the resonance to 0 ppm . Related IUPAC aqueous standard (0.1 M NaCl in D_2O), this is corresponding to -46.1 ppm .^[38] For T_1 measurements,^[39] saturation recovery was performed. Solid-state NMR simulations were carried out using SIMPSON^[40] by varying the quadrupolar constant, applying zero asymmetry parameter and considering an infinite MAS speed. EPR spectroscopy was carried out on a X-band spectrometer (Bruker ELEXSYS E580) at RT. ICP-OES measurements were performed via a double determination using an ARCOS ICP-OES (Spectro Analytical Instruments, Kleve, Germany) with axial plasma view. The samples were dissolved in aqua regia ($\text{HCl}:\text{HNO}_3$, 3:1).

Electrochemical Measurements and Cell Assembly: All electrochemical measurements were performed using a Biologic VMP3 potentiostat. For the EIS measurement, the electrolyte powder was sandwiched between two ion-blocking conductive carbon-coated aluminium disks ($\varnothing = 7 \text{ mm}$) and pressed inside an SS die set at a uniaxial pressure of $\approx 510 \text{ MPa}$ in order to obtain pellets of 7 mm diameter. The impedance spectra were collected in a Swagelok-type cell in the temperature ranges from 25 to 60°C . The pellets were heated to the required temperature and allowed to rest for a period of 60 min in order to attain steady-state temperature prior to the measurement of the EIS spectrum. EIS of the SE pellets was carried out in the frequency range of 1 MHz to 1 Hz and full-cells were recorded in the frequency range 1 MHz to 10 mHz at a sinusoidal amplitude of 10 mV . Pellet thicknesses for CSC-HT and CSIC are 0.68 and 0.74 mm , respectively. Pellet thicknesses for pristine and air-exposed CSIC samples were 0.74 , 0.74 , and 0.8 mm and the corresponding values for the CSIC-HT samples were 0.72 , 0.69 , and 0.78 mm , respectively.

To determine the electrochemical stability window of the SE, bare CSIC pellets were placed between SS current collectors and tested using LSV at a scan rate of 5 mV s^{-1} . An anodic scan of 0 to 5 V versus SS and a cathodic scan of 0 to -5 V versus SS were performed. Galvanostatic cycling of the ASSB with WOCl_4 CAM was conducted in the voltage range $0.5\text{--}3.9 \text{ V}$, while VCl_3 was cycled between 0.5 and 3.3 V at 0.1 C rate. CV was performed in the potential range of $0.5\text{--}3.9 \text{ V}$ for WOCl_4 versus Li/Li^+ , and VCl_3 was cycled between 0.6 and 2.5 V versus Li/Li^+ , $0\text{--}2.0 \text{ V}$ versus

Li–In/Li⁺–In, 0.1–1.7 V versus Mg/Mg²⁺, and 0.1–1.7 V versus Ca/Ca²⁺ at the scan rates of 0.5 and 2.0 mV s^{−1}

Cell Preparation: Li|SE|VCl₃: 180 mg of CSiC powder was poured into a 13 mm diameter stainless steel die set by Specac and initially pressed at 50 MPa. Approximately 2 mg of cathode composite powder consisting of VCl₃, CSiC, and SuperP carbon in the weight ratio 3:6:1 was spread uniformly on one side of the pellet. The SE and the cathode composite were then pressed together at 360 MPa to form a bilayer pellet. Following this, a Li disk of 300 μm thickness and 7 mm diameter was added to the other side of the pellet, along with a 13 mm diameter LDPE film to avoid direct contact of lithium with the steel of the piston and the pellet was pressed again at ≈50 MPa to stick the lithium on the surface of the pellet. Care was taken to prevent lithium from touching the walls of the stainless-steel die set to avoid short-circuit during pellet preparation due to spreading of lithium. The pellet was removed from the die set following the tri-layer pellet preparation. The Li foil|CSiC|WOCl₄ pellet was made similarly for the CV experiment. However, for the cycling experiment, Li foil|CSiC|WOCl₄ cell was assembled with a similar methodology but with ASC AD cell (Sphere energy) with 8 mm diameter PEEK sleeve in order to apply more pressure during cycling. In this case, 80 mg SE powder, 1.5 mg of the cathode composite, and 3 mm diameter lithium foil were used. The cell was cycled at an internal pressure of ≈60 MPa.

Li|In|SE|VCl₃: The preparation steps for the bilayer pellet made of cathode composite and CSiC were the same for the full-cell pellet with Li–In anode. For the preparation of the lithium–indium alloy, foils with Li:In atomic ratio were <1, a lithium disk of 7 mm diameter was punched out of a lithium foil which was pressed to a thickness of less than 100 μm and placed on top of an indium disk of 7 mm diameter and 125 μm thickness. The foils were later pressed together at 240 MPa by placing them inside an LDPE plastic bag to avoid direct contact with the press. After this, a 7 mm disk was punched out of the Li–In alloy foil and placed on the bare side of the bilayer pellet prepared earlier. The final tri-layer pellet with Li–In, SE, and VCl₃ cathode composite layers was pressed at a final pressure of 360 MPa.

Mg|SE|VCl₃: A 10 mm Mg foil was placed at the bottom of the 13 mm diameter SS die. Around 180 mg of CSiC powder was poured on top of the Mg foil and initially pressed at 50 MPa. Approximately 2 mg of cathode composite powder consisting of VCl₃, CSiC, and SuperP carbon in the weight ratio 3:6:1 was spread uniformly on top side of the pellet. The SE, Mg foil, and the cathode composite tri-layer was then pressed together at 360 MPa to form the final pellet.

Ca|SE|VCl₃: The preparation steps for this cell were similar to that of the cell with Mg anode. Here, a 10 mm diameter Ca disk was used.

DFT: In order to investigate the impact of In doping on phase stability and kinetics of CSC, DFT calculations were performed, using the Vienna ab initio simulation package (VASP). VASP is a periodic plane wave code, which allows for an effective description of the electron–ion interaction by pseudopotentials.^[34] Spin-polarized calculations were conducted using the projector augmented wave method, with exchange and correlation being accounted for by the generalized gradient approximation in the formulation of Perdew, Burke, and Ernzerhof.^[35] For the assessment of the impact of In on the energetic stability, 2 × 2 × 2 and 4 × 2 × 2 supercells of the cubic CSC structure were investigated for pristine and In-doped CSC. The doped compounds contained only one In atom per supercell, thus corresponded to CsSn_{0.875}In_{0.125}Cl₃ and CsSn_{0.9375}In_{0.0625}Cl₃ stoichiometries. The structures were optimized with respect to lattice parameters and atomic positions, using an energy cutoff of 400 eV and a 4 × 4 × 4 (2 × 4 × 4) k-point mesh. To assess the relative stability with respect to the competing monoclinic phase-doped and -undoped supercells, the same number of atoms as in case of the cubic structure were investigated. Here, a unit cell with CsSnCl₃ stoichiometry and two In-doped supercells (1 × 1 × 2 and 1 × 2 × 2 supercells of the monoclinic phase) corresponding to CsSn_{0.875}In_{0.125}Cl₃ and CsSn_{0.9375}In_{0.0625}Cl₃ stoichiometry were investigated using a 3 × 6 × 8, 3 × 6 × 4, and 3 × 3 × 4 k-point mesh, respectively.

To gain insights into the kinetics of the material, the barriers for Cl[−] diffusion in both pristine and In-doped cubic CSC were investigated for a 3 × 3 × 3 supercell via the nudged elastic band (NEB) method.^[36] In the case of the In-doped sample, the replacement of one Sn atom

by In corresponded to a CsSn_{0.9815}In_{0.0185}Cl₃ stoichiometry. Finally, for comparison the impact of Sn vacancies was also investigated by removing an additional Sn atom, thus considering CsSn_{0.9815}Vac_{0.0185}Cl₃ and CsSn_{0.963}In_{0.0185}Vac_{0.0185}Cl₃ for the pristine and the In-doped case. Here, it has to be noted that the vacancy on the Sn sublattice was positioned close to the diffusing Cl ion. For all cases, the diffusion path of a Cl ion to a vacant neighboring Cl[−] site was optimized with at least three images between the initial and final state configuration.

Supporting Information

Supporting Information is available from the Wiley Online Library or from the author.

Acknowledgements

The authors gratefully acknowledge the financial support by the Deutsche Forschungsgemeinschaft (DFG, German Research Foundation) under Germany's Excellence Strategy—EXC 2154—Project number 390874152. Part of this work was performed on the HoreKa supercomputer funded by the Ministry of Science, Research and the Arts Baden-Württemberg and by the Federal Ministry of Education and Research. This work contributes to the research performed at CELEST (Center for Electrochemical Energy Storage Ulm-Karlsruhe). G.K. acknowledges the help of Remi Blinder in EPR measurement and Tobias Braun, for the support in collecting the FIB image.

Open access funding enabled and organized by Projekt DEAL.

Conflict of Interest

The authors declare no conflict of interest

Data Availability Statement

The data that support the findings of this study are available from the corresponding author upon reasonable request.

Keywords

all solid-state batteries, cesium tin chloride, chloride-ion conduction, halide solid electrolytes, ion transport in halide perovskites, solid-state ³⁵Cl NMR

Received: April 1, 2023

Revised: May 5, 2023

Published online:

- [1] a) M. Armand, J. M. Tarascon, *Nature* **2008**, *451*, 652; b) K. Hemalatha, A. S. Prakash, G. K., M. Jayakumar, *J. Mater. Chem.* **2014**, *2*, 1757.
- [2] a) M. Sathiyaa, G. Rousse, K. Ramesha, C. P. Laisa, H. Vezin, M. T. Sougrati, M. L. Doublet, D. Foix, D. Gonbeau, W. Walker, A. S. Prakash, M. Ben Hassine, L. Dupont, J. M. Tarascon, *Nat. Mater.* **2013**, *12*, 827; b) M. Sathiyaa, K. Ramesha, G. Rousse, D. Foix, D. Gonbeau, K. Guruprakash, A. S. Prakash, M. L. Doublet, J. M. Tarascon, *Chem* **2013**, *49*, 11376.
- [3] a) G. Karkera, A. S. Prakash, *ACS Appl. Mater. Interfaces* **2019**, *11*, 27870; b) X. Gao, X. Zheng, Y. Tsao, P. Zhang, X. Xiao, Y. Ye, J. Li, Y. Yang, R. Xu, Z. Bao, Y. Cui, *J. Am. Chem. Soc.* **2021**, *143*, 18188; c) G. Karkera, A. S. Prakash, *ACS Appl. Energy Mater.* **2018**, *1*, 1381.

- [4] a) K. Wang, Q. Ren, Z. Gu, C. Duan, J. Wang, F. Zhu, Y. Fu, J. Hao, J. Zhu, L. He, C.-W. Wang, Y. Lu, J. Ma, C. Ma, *Nat. Commun.* **2021**, *12*, 4410; b) N. Tanibata, S. Takimoto, K. Nakano, H. Takeda, M. Nakayama, H. Sumi, *ACS Mater. Lett.* **2020**, *2*, 880; c) S. A. Pervez, B. P. Vinayan, M. A. Cambaz, G. Melinte, T. Diemant, T. Braun, G. Karkera, R. J. Behm, M. Fichtner, *J. Mater. Chem.* **2020**, *8*, 16451; d) L. Lin, K. Wang, A. Sarkar, C. Njel, G. Karkera, Q. Wang, R. Azmi, M. Fichtner, H. Hahn, S. Schweidler, B. Breitung, *Adv. Energy Mater.* **2022**, *12*, 2103090.
- [5] L. Zhou, T.-T. Zuo, C. Y. Kwok, S. Y. Kim, A. Assoud, Q. Zhang, J. Janek, L. F. Nazar, *Nat. Energy* **2022**, *7*, 83.
- [6] T. K. Schwietert, V. A. Arszewlewska, C. Wang, C. Yu, A. Vasileiadis, N. J. J. de Klerk, J. Hageman, T. Hupfer, I. Kerkamm, Y. Xu, E. van der Maas, E. M. Kelder, S. Ganapathy, M. Wagemaker, *Nat. Mater.* **2020**, *19*, 428.
- [7] S. Wang, Q. Bai, A. M. Nolan, Y. Liu, S. Gong, Q. Sun, Y. Mo, *Angew. Chem., Int. Ed.* **2019**, *58*, 8039.
- [8] Y. Xiao, Y. Wang, S.-H. Bo, J. C. Kim, L. J. Miara, G. Ceder, *Nat. Rev. Mater.* **2020**, *5*, 105.
- [9] G. Zhu, X. Tian, H.-C. Tai, Y.-Y. Li, J. Li, H. Sun, P. Liang, M. Angell, C.-L. Huang, C.-S. Ku, W.-H. Hung, S.-K. Jiang, Y. Meng, H. Chen, M.-C. Lin, B.-J. Hwang, H. Dai, *Nature* **2021**, *596*, 525.
- [10] J. Wang, S. L. Dreyer, K. Wang, Z. Ding, T. Diemant, G. Karkera, Y. Ma, A. Sarkar, B. Zhou, M. V. Gorbunov, A. Omar, D. Mikhailova, V. Presser, M. Fichtner, H. Hahn, T. Brezesinski, B. Breitung, Q. Wang, *Mater. Futures* **2022**, *1*, 035104.
- [11] Z. Meng, A. Reupert, Y. Tang, Z. Li, G. Karkera, L. Wang, A. Roy, T. Diemant, M. Fichtner, Z. Zhao-Karger, *ACS Appl. Mater. Interfaces* **2022**, *14*, 54616.
- [12] F. Gschwind, D. Steinle, D. Sandbeck, C. Schmidt, E. von Hauff, *ChemistryOpen* **2016**, *5*, 525.
- [13] C. Chen, T. Yu, M. Yang, X. Zhao, X. Shen, *Adv. Sci.* **2019**, *6*, 1802130.
- [14] N. Nunotani, M. R. I. B. Misran, M. Inada, T. Uchiyama, Y. Uchimoto, N. Imanaka, *J. Am. Ceram. Soc.* **2020**, *103*, 297.
- [15] R. Sakamoto, N. Shirai, A. Inoishi, S. Okada, *ChemElectroChem* **2021**, *8*, 4441.
- [16] I. V. Murin, O. V. Glumov, N. A. Mel'nikova, *Russ. J. Electrochem.* **2009**, *45*, 411.
- [17] T. Xia, Y. Li, L. Huang, W. Ji, M. Yang, X. Zhao, *ACS Appl. Mater. Interfaces* **2020**, *12*, 18634.
- [18] Z. Wu, Q. Zhang, B. Li, Z. Shi, K. Xu, Y. Chen, Z. Ning, Q. Mi, *Chem. Mater.* **2019**, *31*, 4999.
- [19] M. A. Green, A. Ho-Baillie, H. J. Snaith, *Nat. Photonics* **2014**, *8*, 506.
- [20] Z. X. Shen, W. L. Loo, M. H. Kuok, S. H. Tang, *J. Mol. Struct.* **1994**, *326*, 69.
- [21] Z. Rao, W. Liang, H. Huang, J. Ge, W. Wang, S. Pan, *Opt. Mater. Express* **2020**, *10*, 1374.
- [22] Z. Hong, D. Tan, R. A. John, Y. K. E. Tay, Y. K. T. Ho, X. Zhao, T. C. Sum, N. Mathews, F. Garcia, H. S. Soo, *iScience* **2019**, *16*, 312.
- [23] G. Jo, W.-K. Hong, J. Maeng, T.-W. Kim, G. Wang, A. Yoon, S.-S. Kwon, S. Song, T. Lee, *Colloids Surf., A* **2008**, *313–314*, 308.
- [24] G. Karkera, M. Soans, B. Dasari, E. Umeshbabu, M. A. Cambaz, Z. Meng, T. Diemant, M. Fichtner, *Energy Technol.* **2022**, *10*, 2200193.
- [25] G. Karkera, M. A. Reddy, M. Fichtner, *J. Power Sources* **2021**, *481*, 228877.
- [26] Y. Wang, J. Ju, S. Dong, Y. Yan, F. Jiang, L. Cui, Q. Wang, X. Han, G. Cui, *Adv. Funct. Mater.* **2021**, *31*, 2101523.
- [27] R. Matsuda, T. Kokubo, N. H. H. Phuc, H. Muto, A. Matsuda, *Solid State Ionics* **2020**, *345*, 115190.
- [28] X. Chen, Z. Guan, F. Chu, Z. Xue, F. Wu, Y. Yu, *InfoMat* **2022**, *4*, e12248.
- [29] A. Hayashi, H. Muramatsu, T. Ohtomo, S. Hama, M. Tatsumisago, *J. Mater. Chem.* **2013**, *1*, 6320.
- [30] X. Li, J. Liang, J. Luo, M. Norouzi Banis, C. Wang, W. Li, S. Deng, C. Yu, F. Zhao, Y. Hu, T.-K. Sham, L. Zhang, S. Zhao, S. Lu, H. Huang, R. Li, K. R. Adair, X. Sun, *Environ. Sci.* **2019**, *12*, 2665.
- [31] Y. Nikodimos, C.-J. Huang, B. W. Taklu, W.-N. Su, B. J. Hwang, *Environ. Sci.* **2022**, *15*, 991.
- [32] K. Kaup, K. Bishop, A. Assoud, J. Liu, L. F. Nazar, *J. Am. Chem. Soc.* **2021**, *143*, 6952.
- [33] L. M. Riegger, S.-K. Otto, M. Sadowski, S. Jovanovic, O. Kötz, S. Harm, L. G. Balzat, S. Merz, S. Burkhardt, F. H. Richter, J. Sann, R.-A. Eichel, B. V. Lotsch, J. Granwehr, K. Albe, J. Janek, *Chem. Mater.* **2022**, *34*, 3659.
- [34] K. Kanamura, H. Tamura, Z.-I. Takehara, *J. Electroanal. Chem.* **1992**, *333*, 127.
- [35] H. Van Doveren, J. A. T. H. Verhoeven, *J. Electron Spectrosc. Relat. Phenom.* **1980**, *21*, 265.
- [36] N. G. Krishnan, W. N. Delgass, W. D. Robertson, *J. Phys. F: Met. Phys.* **1977**, *7*, 2623.
- [37] J. F. Moulder, W. F. Stickle, P. E. Sobol, K. D. Bomben, in *Handbook of X-Ray Photoelectron Spectroscopy*, Physical Electronics Division, Perkin-Elmer Corp, Norwalk **1995**.
- [38] a) R. P. Chapman, C. M. Widdifield, D. L. Bryce, *Prog. Nucl. Magn. Reson. Spectrosc.* **2009**, *55*, 215; b) R. K. Harris, E. D. Becker, S. M. Cabral de Menezes, R. Goodfellow, P. Granger, *Solid State Nucl. Magn. Reson.* **2002**, *22*, 458.
- [39] K. Yamada, K. Isobe, E. Tsuyama, T. Okuda, Y. Furukawa, *Solid State Ionics* **1995**, *79*, 152.
- [40] a) M. Bak, J. T. Rasmussen, N. C. Nielsen, *J. Magn. Reson.* **2000**, *147*, 296; b) A. Abragam, *Principles of Nuclear Magnetism*, Oxford University Press, Oxford **2011**.